remote sensing

MDPI

Article

Mapping Building Construction Year from Landsat in Data-Scarce, Cloud-Prone Regions: A Parsimonious Spatial Triage Tool for Physical Vulnerability Screening

Yang Liu [1], Xuan Zhang [1], Zewen Mo [1], Zhipang Wang [2] and Qingling Zhang [1,*]

[1] School of Aeronautics and Astronautics, Sun Yat-sen University, Shenzhen 518107, China; liuy975@mail2.sysu.edu.cn (Y.L.); zhangx958@mail2.sysu.edu.cn (X.Z.); mozw9@mail.sysu.edu.cn (Z.M.)
[2] School of Aeronautical Engineering, Changsha University of Science and Technology, Changsha 410114, China; wangzhp25@csust.edu.cn
* Correspondence: zhangqling@mail.sysu.edu.cn

Highlights

What are the main findings?

- A parsimonious framework is developed for building construction year mapping in cloud-prone regions, leveraging annual Landsat NDVI and open footprints via TTM algorithm.
- Validated across two heavily cloud-contaminated metros (Shenzhen, Hanoi), it delivers high accuracy and nearly 1.8-fold improvement over monthly LandTrendr in Shenzhen.

What is the implication of the main finding?

- Coarser but consistent annual composites outperform finer-grained alternatives for built-up change detection under persistent cloud cover.
- This scalable spatial triage tool supports physical vulnerability screening, seismic risk modeling, and resilient planning in resource-constrained, fast-growing regions.

Abstract

Assessing urban resilience requires accurate data on building age as a temporal proxy associated with structural vulnerability, yet persistent cloud cover and rapid development constrain data availability in tropical and subtropical regions. We propose a computationally efficient framework that prioritizes annual data integrity over monthly granularity to map building construction years. By combining annual cloud-free Landsat NDVI (Normalized Difference Vegetation Index) composites with open-source building footprints, the framework utilizes a Temporal Template Matching (TTM) algorithm to detect the distinct "vegetation-to-built" transition signal. Evaluated across two dynamic and heavily cloud-contaminated metropolitan areas—Shenzhen, China, and Hanoi, Vietnam—this approach achieves a high producer's accuracy; furthermore, in Shenzhen, where a monthly comparative analysis was conducted, it outperforms a noise-sensitive monthly LandTrendr-based baseline by a factor of nearly 1.8. Our findings demonstrate that under persistent cloud contamination, a coarser but consistent annual composite provides a more reliable signal than finer-grained alternatives. This scalable methodology generates critical building-age datasets, offering foundational structural intelligence for potential inputs into seismic risk modeling and resilient urban planning in rapid-growth and resource-constrained regions.

Check for updates

Academic Editor: Massimiliano Pepe

Received: 22 May 2026
Revised: 25 June 2026
Accepted: 26 June 2026
Published: 2 July 2026

Copyright: © 2026 by the authors. Licensee MDPI, Basel, Switzerland. This article is an open access article distributed under the terms and conditions of the Creative Commons Attribution (CC BY) license.

Keywords: building construction year; Landsat time series; annual NDVI composites; temporal template matching; cloud-free remote sensing; urban vulnerability; resilient city planning

1. Introduction

The increasing frequency and intensity of natural hazards, exacerbated by climate change and rapid urbanization, pose a severe threat to global stability and sustainable development [1]. International agreements, such as the Sendai Framework for Disaster Risk Reduction, call for a significant enhancement of global capacity to assess and mitigate these risks, particularly in highly vulnerable urban environments of the Global South [2–4]. Within the paradigm of urban resilience, a core tenet is the accurate, spatially explicit assessment of the physical vulnerability of the built environment [5–8]. A building's age serves as a first-order proxy for this vulnerability, as it simultaneously encodes the design standards (e.g., seismic codes, wind-load standards) applicable at the time of construction, the trajectory of material degradation, and the cumulative effects of structural aging [9–15]. Consequently, filling the informational gap regarding building construction years is a prerequisite for subsequent vulnerability modeling and resilient infrastructure planning. Yet, reliable, building-level age data remain largely absent, incomplete, or inaccessible for the vast majority of data-scarce regions that are often most at risk [16,17].

Building upon these mapping capabilities, remote sensing-based retrieval of building construction years has advanced significantly, shifting from macro-scale urban expansion detection to individual building-level age tracking. Current methodologies primarily follow two paradigms: snapshot-based structural feature classification and dense time-series trajectory analysis.

The first paradigm leverages advanced machine learning and deep learning architectures-such as convolutional neural networks (CNNs) and semantic segmentation workflows-applied to high-resolution imagery or multi-source remote sensing data. By integrating optical imagery with synthetic aperture radar (SAR) and airborne Light Detection and Ranging (LiDAR), these approaches estimate building age from morphological attributes, including roofing materials, architectural typologies, and structural heights [18,19]. Multi-temporal feature classification workflows further combine spectral, textural, and structural metrics derived from multi-sensor data (e.g., Landsat, Sentinel-1/2, and Nighttime Light data) to predict or back-cast construction periods [20]. Although effective for localized mapping at specific timestamps, these frameworks remain highly dependent on extensive volumes of annotated training samples. Consequently, their geographical transferability faces operational constraints when scaled across heterogeneous landscapes or applied to historical periods where high-resolution data are unavailable.

To address the limitations of snapshot-based mapping over long historical periods, a separate research direction focuses on dense satellite time-series analysis to determine the temporal onset of construction. Facilitated by the opening of historical satellite archives, particularly the Landsat data which provides extensive temporal depth spanning the past four decades, researchers track the continuous spectral trajectory of specific pixels or building objects [21]. By analyzing distinct change-points that characterize the transition from natural pervious surfaces (such as vegetation or bare soil) to impervious built structures, these frameworks capture the abrupt surface reflectance shifts caused by building construction. Within this domain, trajectory-based change detection algorithms originally designed for vegetation and ecological disturbance monitoring—such as Landsat-based Detection of Trends in Disturbance and Recovery (LandTrendr), Continuous Change Detection and

Classification (CCDC), and BFAST—have been adapted to reconstruct decades of urban building age [22–25].

Despite the high temporal precision offered by continuous observation, this time-series paradigm encounters operational limitations in persistently cloudy tropical and subtropical zones, such as parts of Southeast Asia and Central Africa, where atmospheric contamination introduces chronic data omissions [26,27]. Such data-scarce conditions can disrupt the temporal continuity required by time-series algorithms, potentially leading to increased noise, elevated rates of false detections, and a subsequent degradation in model performance [28]. This introduces a critical methodological mismatch: continuous time-series methods optimized for high temporal tracking exhibit reduced robustness in cloud-prone regions where regional data limitations are most pronounced.

To address these limitations, we propose a robust and methodologically parsimonious framework. We deliberately move away from unreliable high-frequency signals. Instead, our framework leverages two key components: (1) the generation of cloud-free annual NDVI composites, which prioritize data integrity over temporal resolution, and (2) a Temporal Template Matching (TTM) algorithm, adapted from industrial land-cover monitoring logic [29], that identifies the characteristic "vegetation-to-built" transition signature from coarse-grained but consistent annual signals. We do not claim algorithmic complexity as our primary contribution; rather, the deliberate simplicity of this framework—which avoids deep learning pipelines and extensive training data requirements—is central to its utility in resource-constrained settings. By offering a computationally lightweight methodology that operates efficiently on open-source platforms with publicly available data, this work generates previously unavailable building-age datasets, providing foundational structural-level intelligence as potential inputs for seismic risk modeling, proxy-based vulnerability screening, and resilient urban planning.

2. Materials and Methods

2.1. Study Area and Data

2.1.1. Study Areas

To evaluate the generalizability and robustness of the proposed method across different urban development contexts and climatic conditions, two representative metropolitan areas were selected as study areas: Shenzhen (China) and Hanoi (Vietnam). These two cities exhibit distinct characteristics in terms of economic structures, administrative planning, and environmental constraints, collectively reflecting the diversity and complexity of rapid urban landscape transformations in contemporary Asia (see Figure 1).

Shenzhen, a premier megacity in southern China, represents a distinctive case of profound economic growth and hyper-rapid urbanization. Over the past few decades, Shenzhen has transitioned from a substantial horizontal "incremental expansion" to an intensive "stock land optimization" and urban renewal stage. Testing the model in Shenzhen serves to verify its sensitivity and precision in capturing high-density, high-intensity construction dynamics within a mature and rapidly evolving statutory urban environment. Furthermore, as Shenzhen is selected for the comparative monthly baseline analysis, it provides a rigorous testbed for evaluating the model's computational efficiency and algorithmic stability.

Hanoi, the capital of Vietnam, offers a compelling counterpart that showcases a policy-driven and administrative boundary-induced urban trajectory. Situated in a tropical monsoon zone, Hanoi is characterized by persistent cloud cover throughout the year. The inherent challenges of severe data gaps and cloud contamination in this region frequently constrain traditional remote sensing observations. Therefore, incorporating Hanoi into the study allows for a rigorous validation of the proposed annual composite method's time-series reconstruction capability and its resilience against persistent atmospheric noise.

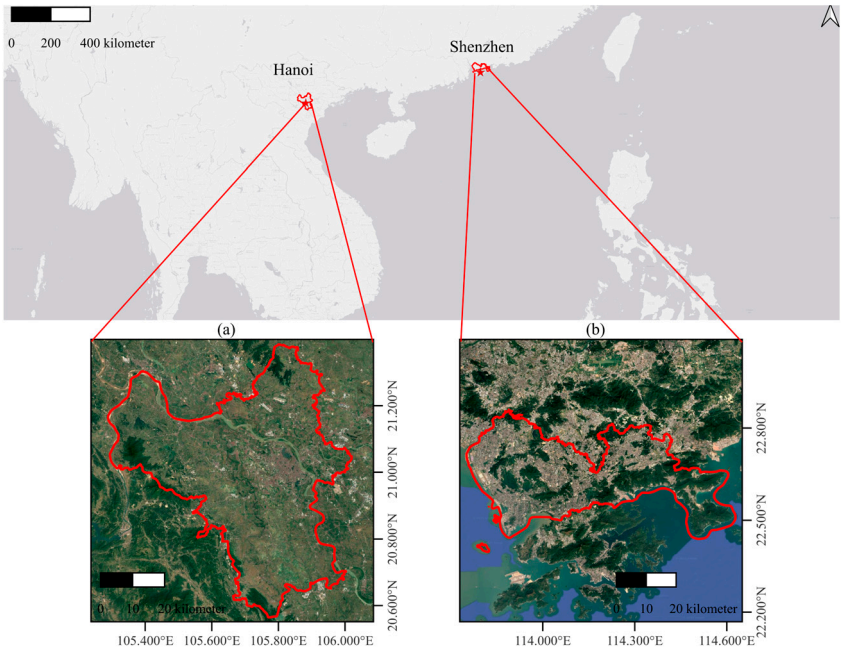


Figure 1. Locations of the two study areas: (**a**) Hanoi, Vietnam, and (**b**) Shenzhen, China.

2.1.2. Satellite Data

Table 1 shows the types of datasets used in this paper. The Landsat program, a joint scientific initiative between the National Aeronautics and Space Administration (NASA) and the United States Geological Survey (USGS), has systematically acquired global land remote sensing data for decades, providing a long-term continuous observation archive. This study used data from two satellite missions: Landsat 7, launched in 1999 and carrying the Enhanced Thematic Mapper Plus (ETM+), and Landsat 8, launched in 2013 and equipped with the Operational Land Imager (OLI) and the Thermal Infrared Sensor (TIRS). Both satellites operate in sun-synchronous orbits, achieving global coverage every 16 days at a spatial resolution of 30 m. Their stable spatial resolution and spectral characteristics make them particularly suitable for land cover change analysis [30].

Table 1. The remote sensing data used in this study.

Data Set	Data Name	Spatial Resolution	Date	Source
Landsat	Landsat-7/ETM+	30 m	11 January 2000–16 November 2021	GEE [1]
	Landsat-8/OLI	30 m	15 January 2014–10 December 2021	GEE
High-resolution data	DigitalGlobe Imagery	0.6–1.0 m (2000–2010) 0.3–0.5 m (2011–2020)	2000–2020	Google Earth
Building Footprints	Google Open Buildings (v3)	/	2021–Present	Google Research

[1] Google Earth Engine (USGS).

To assess the accuracy of building extraction, Google Earth historical imagery spanning 2000 to 2020 with a 1–2-year temporal interval was utilized as an independent validation dataset. The spatial resolution of this dataset exhibits marked spatio-temporal heterogeneity and inter-city differences: in Shenzhen, the resolution ranges from 0.6 to 1.0 m during 2000–2010 and improves to sub-meter levels of 0.3 to 0.5 m after 2011; in Hanoi, the resolution is approximately 1.0 to 2.4 m during the early period (2000–2008) and stabilizes around 0.5 m after 2009. It should be noted that during the early 2000s, due to the limited deployment and limited revisit temporal frequencies of commercial high-resolution satellite

constellations, years lacking clear high-resolution overpasses defaulted to a coarse 30 m resolution filled by medium-resolution Landsat mosaics, which reduced the spatial detail of the imagery during these specific historical intervals [31]. For quality control, global cloud cover was strictly constrained to less than 5% for all validated high-resolution windows, and images were predominantly acquired during cloud-free winter and spring months.

The Open-Buildings dataset, developed by Google Research, extracts building features from high-resolution satellite imagery [32,33]. This dataset primarily covers Africa, South Asia, Southeast Asia, and Latin America, comprising approximately 1.8 billion detected building footprints. Each record includes a geometric polygon defining the building outline, a confidence score, and a Plus Code corresponding to its centroid. In this study, we integrated these high-resolution building vector datasets from Google to enhance spatial precision and facilitate analysis at the individual building level.

2.2. Methodology

Figure 2 illustrates the overall framework of the proposed method for reconstructing building construction age sequences. The framework consists of three core modules multi-source data harmonization and preprocessing, temporal feature modeling via the Gaussian-Manhattan Algorithm, and result validation with accuracy assessment. In the initial preprocessing stage, the system integrates multi-temporal imagery from Landsat-7 and Landsat-8 satellites spanning from 2000 to 2020. To reduce cloud contamination and ensure temporal continuity, a dynamic rolling-window compositing strategy was adopted. Specifically, this strategy selects clear-sky observations from key vegetation phenological stages each year to generate a 20-year cloud-free NDVI annual composite sequence, thereby ensuring the data integrity and the comparability required for subsequent change detection.

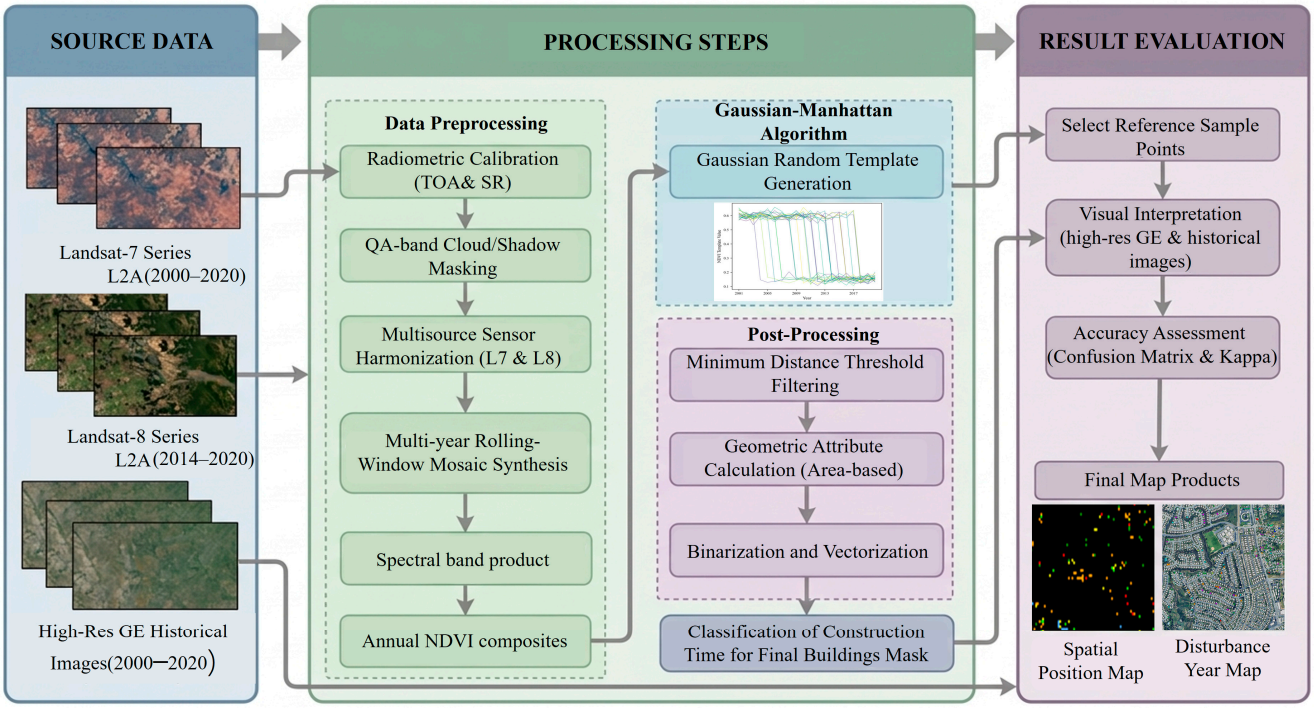


Figure 2. The comprehensive methodological workflow, comprising source data acquisition, core processing steps, and result evaluation. In the Gaussian Random Template Generation panel, different colors represent NDVI trajectory templates with disturbance events occurring in different years. In the Spatial Position Map, different colors represent the spatial distribution of detected transition locations. In the Disturbance Year Map, different colors indicate the specific year identified for each pixel as having undergone the vegetation-to-built transition.

2.2.1. Preprocessing: Generation of Robust Annual NDVI Composites

We used GEE to process the top-of-atmosphere (TOA) data from Landsat 7/8 Collection 1. The gaps in SLC-off imagery were filled [34], and the Landsat 8 data were harmonized with Landsat 7 to ensure consistency [35]. All images were masked for clouds and shadows using the QA bands.

Although having certain drawbacks, the Maximum NDVI Value method is straightforward, simple, and quick, allowing NDVI compositing at a broad scale, even at the global scale, and can ensure high-quality data from the growing season. In this study, we adopted the mixed NDVI composite approach proposed by Zhang et al. [36], adapted from the Maximum NDVI Value method and generated NDVI composites on GEE using various treatments for vegetation, barren land, and water.

We first established two thresholds for distinguishing vegetation (maximum NDVI > 0.4) and water bodies (minimum NDVI < −0.3) from others. Then, we generated a composite with median NDVI and replaced all median NDVI values more than 0.4 with the Maximum NDVI value in the NDVI image collection and all values less than −0.3 with the minimum NDVI value. This method successfully mitigates the effects of some seasonal and transitory variations in feature categories. In addition, we multiplied each pixel's final NDVI value by 10,000 and transform it to an int16 integer to reduce file storage space. Finally, we obtained an annual mixed NDVI composite.

Consequently, through this annual pixel-based optimization and rolling composite approach, the specific calendar dates of individual image overpasses become less critical. Since our refined research scope now focuses exclusively on Shenzhen and Hanoi—both located in the Northern Hemisphere and sharing relatively synchronized, yet slightly varying, subtropical/tropical growing seasons—this annual integrated NDVI composition effectively suppresses localized seasonal peaks and transitory phenological noise. It ensures that the derived NDVI matrices capture the stable, long-term persistent impervious surfaces and vegetative backgrounds rather than intra-annual seasonal fluctuations, ensuring rigorous geographic comparability between the two target cities.

To address temporal gaps caused by cloud cover, a rolling compositing strategy was applied—a 3-year temporal window was used for 2000–2013 (Landsat 7 data), and a 2-year window was used from 2014 onward (Landsat 8 data), as shown in Figure 3. Although this introduces a lag effect of 1 to 2 years, it increases pixel availability and temporal continuity in cloudy regions, generating a stable and coherent NDVI time series suitable for detecting construction-induced surface transitions.

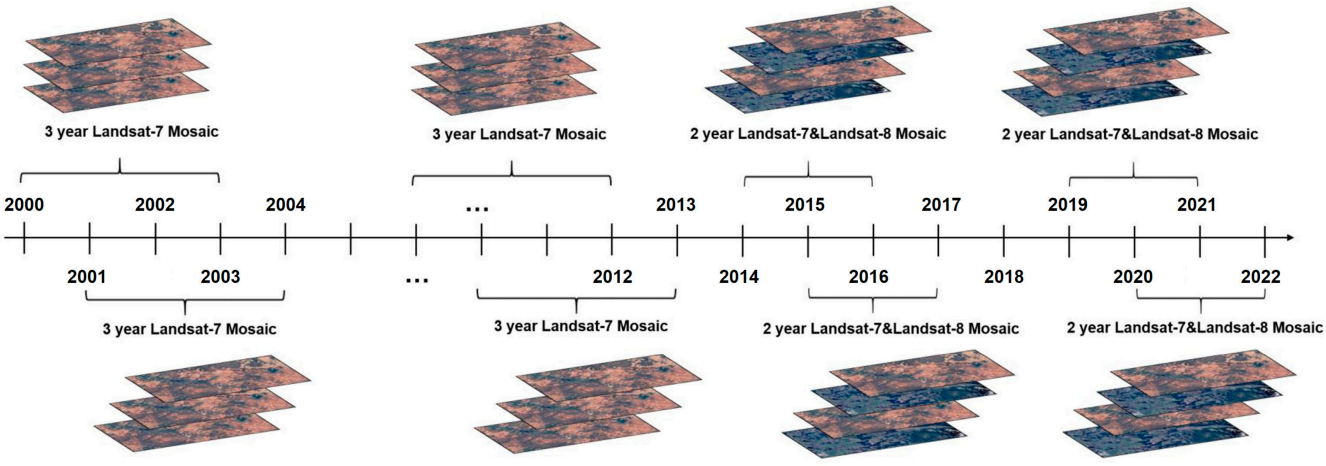


Figure 3. Schematic of the adaptive rolling-window mosaic synthesis strategy for time-series image generation.

2.2.2. Temporal Template Matching (TTM) for Construction Year Detection

To mitigate misclassification risks arising from the complexity of land cover types and the limited number of templates, the model incorporates a minimum distance threshold mechanism. This threshold serves to distinguish genuine construction pixels from false positives: pixels undergoing pronounced "vegetation-to-building" transitions should exhibit minimum distances below the established threshold, whereas unchanged pixels or false detections typically yield distance values exceeding this threshold. The threshold is confirmed through subsequent validation procedures, maintaining detection sensitivity while reducing false positive rates and thereby enhancing overall classification reliability.

The template matching strategy adopted in this study was adapted from a method originally developed for detecting shale oil and gas well pad construction [29], which assumes that the vegetation-to-bare-ground transition exhibits spectral dynamics at the Landsat pixel scale similar to those of urban building construction. We substantially modified this method for urban environments by constructing a template library containing 20 patterns and combining it with a building footprint mask and a majority voting mechanism to ensure building-level identification accuracy. When monitoring urban surface dynamics, the building construction process typically appears as the removal of existing vegetation cover, replaced by artificial surfaces such as concrete structures. This transition can be identified and quantified through Normalized Difference Vegetation Index (NDVI) time series. As a key indicator of vegetation cover and biomass, NDVI is calculated as:

$$NDVI = \frac{NIR - R}{NIR + R} \quad (1)$$

where NIR represents near-infrared reflectance and R represents red band reflectance. This index is sensitive to chlorophyll content and photosynthetic activity, enabling a distinction between vegetated areas and the built environment. Building activity is therefore characterized by a negative trend in NDVI values over time.

A systematic characterization of change patterns requires first establishing the statistical NDVI behavior of different land cover types across the study region [37]. For this purpose, we collected a total of 1000 high-confidence sample points—500 representing stable vegetation and 500 representing built-up areas—distributed across two highly dynamic metropolitan regions with contrasting geographic and climatic settings: Shenzhen, China, and Hanoi, Vietnam. Long-term historical imagery covering the period 2000–2020 provided the temporal foundation for this sampling. The stable vegetation samples primarily included dense forest, shrubland, and perennial urban green spaces, while the built-up samples encompassed typical impervious surfaces such as residential, industrial, and commercial infrastructure. To eliminate seasonal fluctuations and annual phenological anomalies, the statistics were derived from multi-year composite NDVI trajectories across the two decades, rather than being estimated separately by individual year, season, or city.

The empirical results indicated that across different regions and years, the mean growing-season NDVI of stable vegetation areas consistently hovered around 0.6 ($variance \approx 0.05$), while both newly built and existing building areas exhibited a mean NDVI of approximately 0.15 ($variance \approx 0.05$). Although these values represent macro-level approximations rather than site-specific absolute thresholds, they provide a reliable, generalized quantitative basis for identifying construction dynamics. At the methodological level, this study proposed an improved algorithm that integrates rolling compositing and stochastic simulation within an advanced temporal change detection framework. The method employs a Gaussian random process with observational variance constraints to generate statistically representative NDVI transition templates. Specifically, the system generates random sequences following a Gaussian distribution based on these empirical

baseline anchors, using stochastic perturbations to simulate the localized, heterogeneous building disturbance conditions and dynamic background noise across different geographical sectors. This improvement enhances the physical realism and regional adaptability of the temporal simulation. The final generated template set comprises 20 representative land cover transition patterns (Figure 4c), comprehensively covering possible transition pathways from 2001 to 2020, thereby establishing an interpretable and verifiable mathematical foundation for robustly identifying construction dynamics.

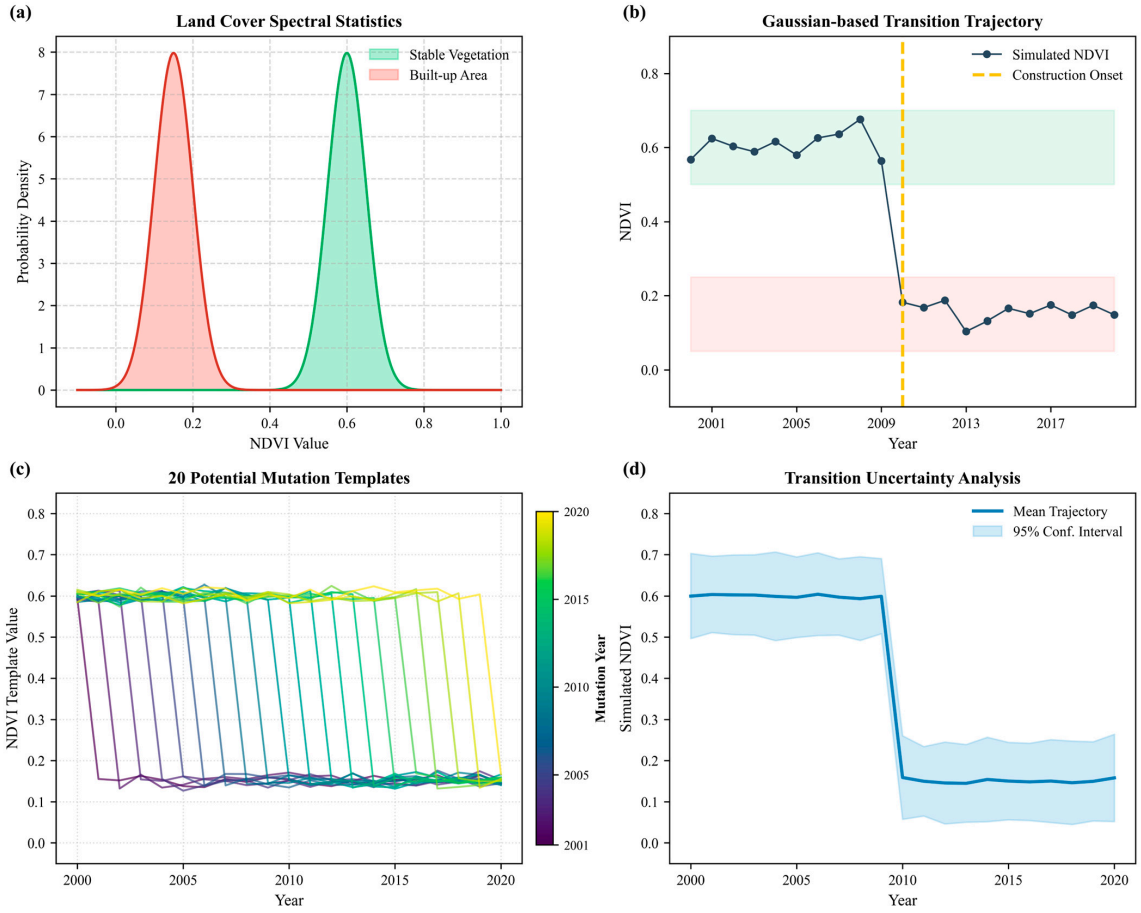


Figure 4. Characterization of NDVI time-series transition patterns and synthetic abrupt-change templates: (**a**) Probability density functions illustrating the spectral separability between stable vegetation and built-up areas; (**b**) a representative Gaussian-based transition trajectory from 2000 to 2020, with the vertical dashed line marking the construction-induced transition onset; (**c**) a library of 20 abrupt-transition templates capturing annual transition events occurring between 2001 and 2020; and (**d**) a transition uncertainty analysis showing the mean trajectory and 95% confidence interval (CI) to account for stochastic noise and temporal variations.

The core computational process of the model employs a minimum distance classification approach to quantify the similarity between observed NDVI time series vectors and predefined classification templates. The classification vectors were constructed from annual NDVI composite images acquired between 2000 and 2020 and matched against the 20 simulated stochastic time series templates, enabling temporal identification of different building construction stages. For the distance metric, Manhattan distance metric was selected in preference to Euclidean distance or cosine similarity [38]. The calculation principle of the Manhattan distance between two dimensional vectors, $X_1 = (a_1, a_2, \ldots, a_n)$ and $X_2 = (b_1, b_2, \ldots, b_n)$, is defined by Equation (2). Characterized by its rectilinear coordinate

geometry, this metric offers distinct computational advantages, notably its high execution speed and simplicity in algorithmic implementation.

$$D(X_1, X_2) = \sum_{K=1}^{n} |a_k - b_k| \tag{2}$$

where a_k and b_k represent the respective components of the n-dimensional vectors across n temporal windows. Thanks to its rectilinear coordinate geometry, this metric enables efficient and robust detection of building construction dynamics within our template matching framework.

At the processing level, because it bypasses the computationally expensive squaring and square root operations characteristic of Euclidean metrics, it achieves high computational efficiency and simplicity in large-scale pixel-level algorithmic implementation on cloud computing platforms like Google Earth Engine. At the analytical level, by computing the sum of absolute linear differences between corresponding time points, the Manhattan distance exhibits greater robustness against outliers, ensuring that random noise from residual cloud cover, shadow contamination, or short-term seasonal phenological fluctuations does not disproportionately distort the overall matching results. In contrast, higher-order alternative metrics like the Euclidean distance, due to their squared terms, nonlinearly amplify or compress data fluctuations within the standard NDVI range of $[-1, +1]$, potentially introducing artificial errors and over-penalizing single-date anomalies. Similarly, directional metrics such as Cosine similarity are fundamentally less sensitive to magnitude differences and are therefore unsuitable for capturing the absolute change amplitude and vertical drops that characterize vegetation-to-built transitions in time series. Adopting the Manhattan distance mitigates such geometric distortion issues, thereby maintaining fidelity in measuring true NDVI trajectory differences during urban expansion.

To support a comprehensive interpretation of the proposed remote sensing detection framework, Figure 4 systematically illustrates the characterization of NDVI time-series transition patterns and the construction of synthetic abrupt-change templates. Specifically, Figure 4a presents the probability density functions of spectral signatures for stable vegetation and impervious surfaces. A distinct, non-overlapping bimodal distribution emerges, indicating strong spectral separability between the vegetated background, which peaks at an NDVI value of approximately 0.6, and impervious surfaces, which peak near 0.15.

Figure 4b shows a representative Gaussian-based transition trajectory derived from a single pixel undergoing urban development. The blue line and markers trace the simulated annual NDVI trajectory from 2001 to 2020. Prior to 2010, the pixel remains in a stable high-NDVI state (shaded green zone), consistent with undisturbed vegetation. A sharp NDVI decline occurs between 2009 and 2010, precisely identified by the vertical yellow dashed line, marking the "Construction Onset" as the exact year of the abrupt transition. Following this transition, NDVI values stabilize at a persistently low level (shaded red zone), indicating the completion of urban sealing.

For modeling all possible temporal variants over the 20-year study period, Figure 4c provides a set of 20 candidate abrupt-transition templates. Each trajectory, color-coded by its transition year from 2001 (dark purple) to 2020 (bright yellow), represents a synthetic and idealized urban transformation pathway.

Finally, Figure 4d addresses inherent stochastic noise and short-term variability, such as seasonal vegetation fluctuations or atmospheric artifacts, through a transition uncertainty analysis. The solid blue line denotes the estimated mean transition trajectory, while the light blue shaded envelope indicates the 95% confidence interval (CI). This uncertainty bounding ensures that the detection algorithm remains robust against individual sensor anomalies or

seasonal phenological noise, thereby ensuring that only genuine anthropogenic land cover transitions are captured.

To reduce misclassification risk introduced by heterogeneous land cover and a limited template set, we incorporated a minimum distance threshold as a core parameter to separate true construction pixels from spurious detections [39]. The underlying reasoning is straightforward: pixels that undergo a clear vegetation-to-building transition tend to produce minimum trajectory distances that fall below a certain critical value, whereas unchanged pixels or those affected by unrelated surface disturbances generally yield distances well above that value.

Following the logic of empirical statistical bounds, we determined these thresholds through a random simulation strategy, which ensures regional relevance while avoiding subjective interference. Within each study area, we randomly drew 400 validated building construction samples and another 400 samples associated with other types of surface disturbance—such as agricultural dynamics or bare land fluctuation—and then characterized their minimum distance distributions over 5000 empirical simulation runs.

To define the "optimal threshold" explicitly, candidate thresholds were swept across the observed range of minimum-distance values. For each candidate threshold τ, pixels with a minimum distance lower than τ were classified as construction pixels, while those exceeding τ were regarded as false construction detections or non-construction disturbances. Precision, recall, and F1-score were then calculated against the validated construction and non-construction labels. The optimal threshold was defined as the value that maximized the F1-score, thereby balancing omission and commission errors. When multiple candidate thresholds produced comparable F1-scores, the lower threshold was selected to further suppress false positives.

As shown in Figure 5, the two simulated minimum-distance distributions exhibit clear statistical separation between true construction pixels and false construction pixels. Based on the maximum F1-score criterion, the optimal thresholds were identified as 12,500 for Shenzhen (Figure 5a) and 11,400 for Hanoi (Figure 5b). In practice, pixels with a minimum distance below the region-specific threshold retained their construction label, whereas pixels exceeding the threshold were reassigned to other classes.

2.2.3. Aggregation and Validation

Building footprint data from the Open-Buildings and Microsoft Building Footprint datasets were integrated to filter and mask non-building areas, thereby constraining the spatial computational domain prior to the intensive NDVI trajectory-matching process. To address the mixed-pixel problem inherent in medium-resolution (30 m) Landsat imagery and the spectral heterogeneity within building footprints, a decision fusion strategy based on the majority rule was applied [40].

To transition pixel-level detection to individual building objects, a refined spatial overlay and aggregation workflow was implemented based on the principle of majority voting. First, the spatial geometry of each building polygon was overlaid and intersected with the gridded Landsat-derived annual construction year map. To ensure statistical robustness, a minimum threshold of valid pixel coverage was established; a building polygon was retained for chronological assignment only if its footprint intersected with at least one valid pixel containing a detected disturbance year. For standard and large building structures that spanned multiple grid cells, we employed an area-weighted majority voting rule. To mitigate spatial discretization bias inherent in unweighted pixel counting, the final construction year $Y_{building}$ allocated to the building polygon was determined by maximizing the total intersecting area, defined as follows:

$$Y_{building} = arg\max_{y} \sum_{i=1}^{N} Ai \cdot \delta(yi,\ y) \tag{3}$$

where Ai represents the intersection area between the building polygon and the i-th pixel, yi is the detected construction year of the i-th pixel, and δ is the Kronecker delta function. For sub-pixel building structures whose total footprint area was smaller than a single Landsat pixel (<900 m^2), the area-weighted voting rule converged to a centroid-based maximum-overlap assignment. Specifically, the building structure was assigned the construction year of the grid cell that contained the geometric centroid of the building polygon.

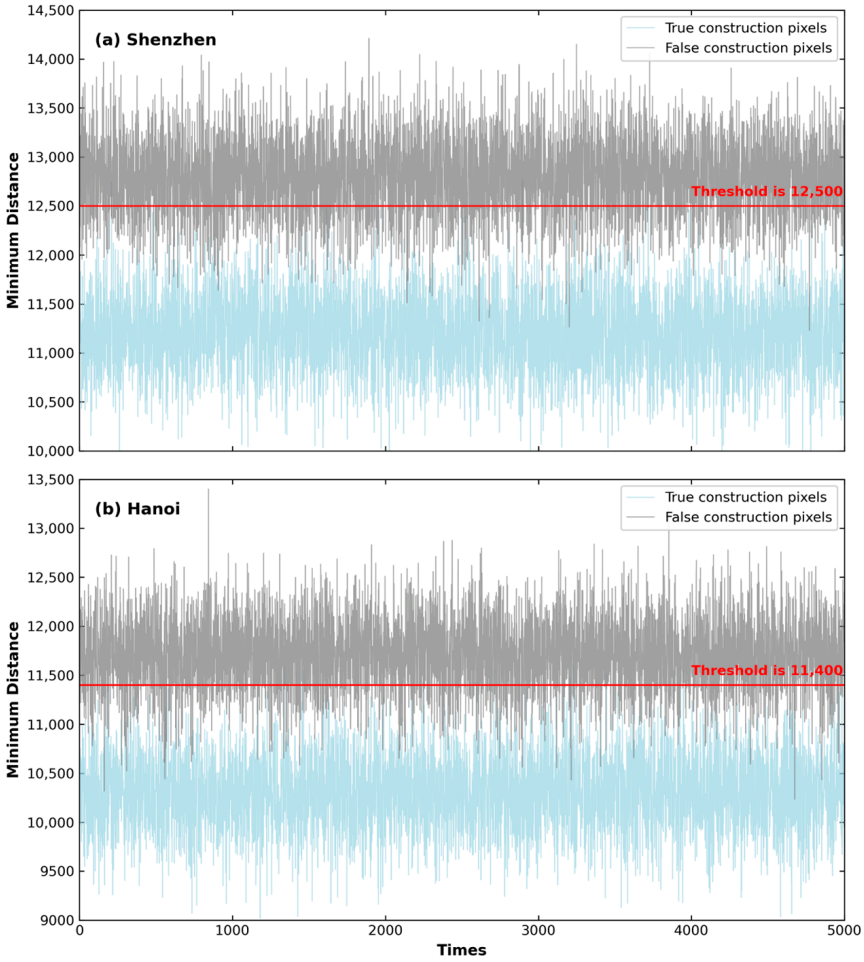


Figure 5. Empirical statistical distributions of minimum-distance metrics derived from 5000 random simulation runs for threshold determination. The red threshold lines indicate the optimal thresholds selected using the maximum F1-score criterion: (**a**) Shenzhen, with an optimal threshold of 12,500; and (**b**) Hanoi, with an optimal threshold of 11,400.

A multi-level validation framework was designed to evaluate the accuracy of the proposed model. Candidate construction sites and their predicted construction years were first identified from the model outputs. To ensure maximum independence and reliability of the validation, we strictly prioritized direct visual interpretation against independent, high-temporal-resolution satellite imagery (Google Earth and other available high-resolution datasets). Every effort was made to exhaust all clear, cloud-free historical imagery to directly verify the temporal alignment between estimated and actual construction timelines.

For regions where imagery quality was compromised, cloud cover was persistent (a common challenge in cloud-prone areas), or structural details were inherently ambiguous in historical imagery, NDVI time series served only as an unavoidable alternative

and supplementary evidence when no other independent high-resolution images were accessible. In these constrained observation conditions, construction initiation typically manifests as an abrupt decline from high to low NDVI values, corresponding to vegetation clearance, followed by stabilization or slight recovery upon construction completion and surface stabilization. Comparing these dynamic NDVI trajectories with model predictions allowed an indirect, passive verification of temporal accuracy. This indirect approach was deployed as a last resort strictly confined to severe data-gap areas, ensuring that the most reference labels remained primarily anchored to independent, direct high-resolution image interpretation.

A confusion matrix served as the primary quantitative evaluation tool, with rows representing reference classes and columns representing predicted classes. From this matrix, overall accuracy, user's accuracy (UA), and producer's accuracy (PA) were derived to provide a multi-dimensional assessment of classification performance. Producer's accuracy—the proportion of reference validation samples correctly identified by the model—was adopted as the primary metric for evaluating the framework's capacity to capture real construction events. To ensure representativeness while balancing the manual verification workload, 90 sampling points were randomly selected from the building footprint data for each study area and year, yielding a total of 3600 validation points across the two cities over the 20-year study period.

To avoid circular validation, the reference labels were primarily established through direct visual interpretation of independent high-resolution Google Earth historical imagery. Among the 3600 validation samples, approximately 2500 samples, or about 70%, were directly interpreted from high-resolution imagery, while approximately 1100 samples, or about 30%, required supplementary NDVI-based verification because clear high-resolution imagery was unavailable or temporally ambiguous. These NDVI-assisted cases were mainly concentrated in the early observation period from 2001 to 2008, when historical high-resolution imagery was often incomplete, cloudy, or insufficiently detailed, although a limited portion of the early samples could still be directly interpreted from usable imagery. After 2009, most samples could be directly verified using high-resolution historical imagery. The NDVI trajectories were therefore used only as auxiliary evidence for reference labeling in data-gap cases, rather than as the primary validation source.

The performance of the proposed framework was evaluated through comparative analyses against two methods representing distinct methodological paradigms. The monthly NDVI-based LandTrendr approach of Hu et al. (2024) [11] and the full-band BATSCCD method of Zhuo et al. (2024) [21] were selected as reference baselines. The specific comparison protocols—including data harmonization procedures and evaluation metrics—are detailed in Section 3.3 alongside the corresponding results.

3. Results

Based on the principle of majority voting, the analysis aggregates within individual building vectors, thereby enabling an exploration of the temporal relationship between NDVI values and the timing of building construction across the studied areas.

Figure 6 presents the macro-scale classification results for the two study areas. To enhance visual interpretability, the construction timeline from 2001 to 2020 was divided into four distinct chronological stages, using a red-to-green color gradient. This specific color scheme was selected to intuitively reflect the relative duration of exposure to environmental stressors, where redder tones indicate earlier construction periods that may possess a higher baseline physical vulnerability.

To offer a more detailed perspective, Figure 7 illustrates selected subregions within these two study areas, emphasizing localized morphological attributes and the precise outcomes of the majority-voting mode analysis. Unlike the staged categorization shown in Figures 6 and 7 applies a year-by-year color assignment, allowing a clear distinction of annual variations and dominant localized deployment characteristics.

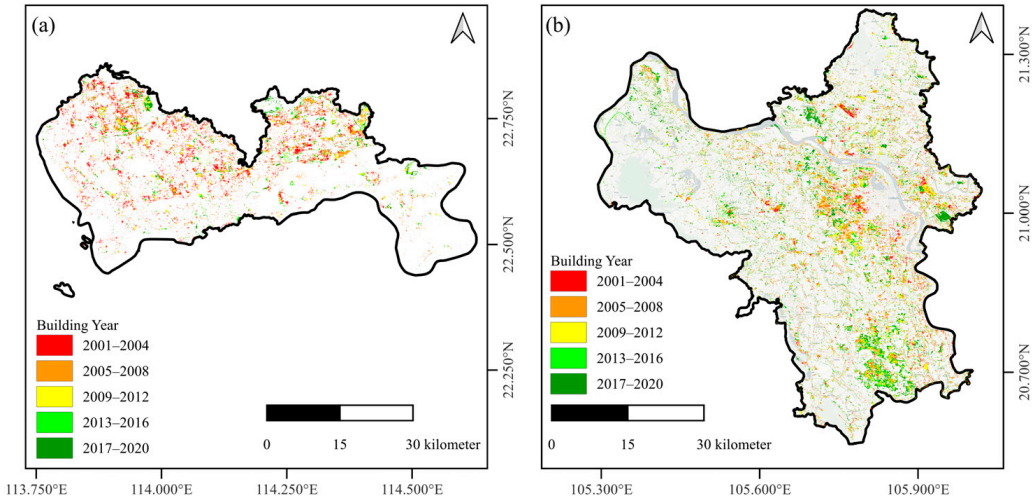


Figure 6. Spatiotemporal distribution of historical construction years across the two study areas categorized into distinct chronological stages: (**a**) Shenzhen, China; and (**b**) Hanoi, Vietnam.

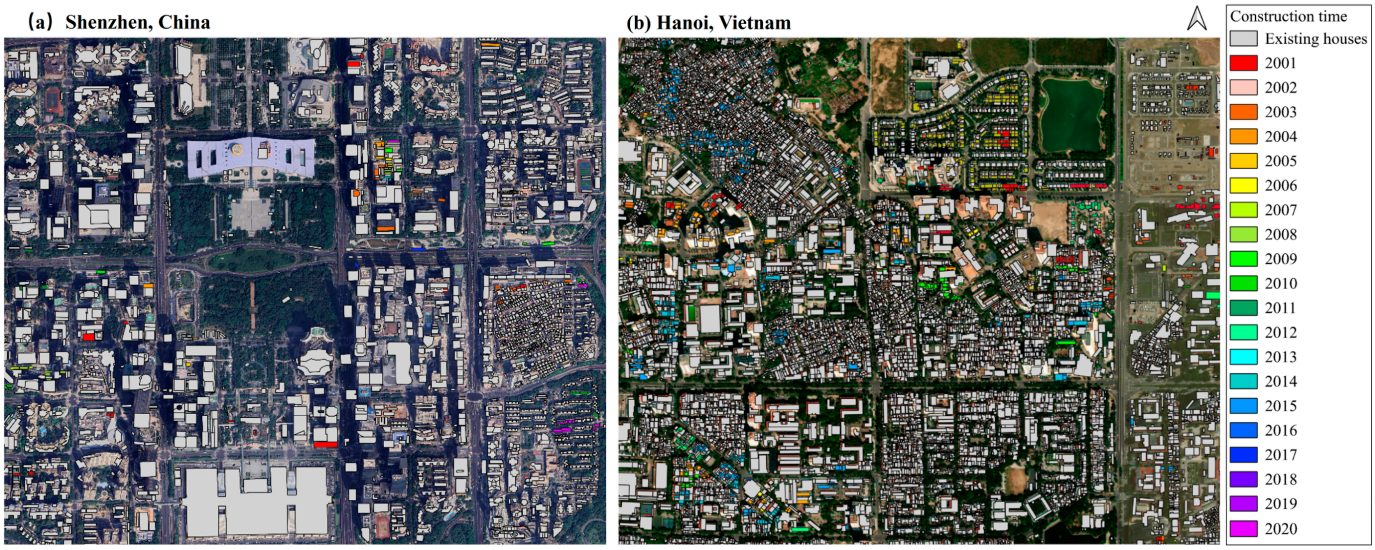


Figure 7. Final categorized map showing detailed changes of sub-areas within the two regions.

Overall, the distinct boundaries and spatially consistent patterns observed in both figures demonstrate that the proposed framework functions reliably and robustly in capturing and resolving the target urban construction dynamics.

The temporal trend observed in Hanoi, Vietnam, exhibits distinctive macroeconomic phases. According to the statistical baseline in Figure 8b, Hanoi experienced a sustained proliferation of new construction activities between 2001 and 2010, with a pronounced singular deceleration captured in 2003. This localized drop in detected construction frequency is primarily attributable to the intrinsic detection mechanics of the proposed framework; building structures erected during this specific year were largely deployed across precleared or non-vegetated surfaces, thereby falling outside the spectral disturbance envelope optimized for vegetation-to-building transitions. Subsequently, from 2011 to 2020, the an-

nual volume of newly registered buildings experienced a noticeable decline—particularly within the 2011–2015 interval—reflecting a temporary deceleration in Hanoi's horizontal urban expansion and a transition toward lower development rates. After 2016, a resurgent trajectory in construction volume emerged, indicating that the municipality had entered a renewed phase of structural urbanization and peripheral expansion.

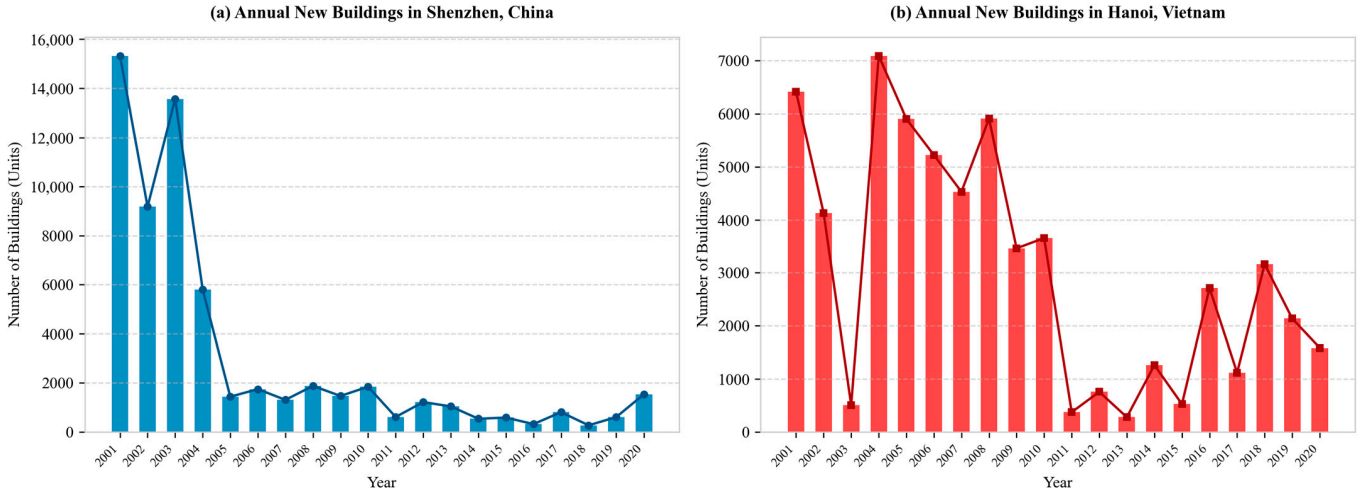


Figure 8. Annual new buildings from 2001–2020 in (**a**) Shenzhen, China and (**b**) Hanoi, Vietnam. Unit: buildings.

Concurrently, as illustrated in Figure 8a, Shenzhen maintained a persistently high volume of new construction from 2001 to 2004. However, a pivotal inflection point occurred in 2005, after which the volume of vegetation-destructive construction exhibited a progressive downward trend. Given that the proposed sensing framework specifically targets urban transformations intersecting with greenfield clearance, this historical shift strongly implies a structural transition in Shenzhen's developmental paradigm. Rather than a slowdown in absolute economic growth, this trend reflects the stringent enforcement of urban ecological redlines alongside a strategic pivot from horizontal greenfield expansion to vertical brownfield redevelopment and urban renewal, successfully aligning territorial modernization with environmental conservation goals.

3.1. Quantitative Accuracy Assessment

The classification accuracy of the proposed framework in predicting building construction timelines was quantitatively assessed using a confusion matrix as the primary validation tool, enabling a multi-faceted evaluation of interconnected accuracy dimensions. Specifically, this study utilizes producer's accuracy (PA) to measure the probability that a specific reference class is correctly classified, thereby reflecting the omission error, whereas user's accuracy (UA) indicates the probability that a pixel assigned to a given category genuinely represents that category on the ground, thereby capturing the commission error. At the macro-scale, the overall accuracy (OA) represents the total proportion of correctly classified sample points across the entire study period, inclusive of the "Unclear" category assigned during manual inspection. Concurrently, the mean absolute error (MAE) and root mean squared error (RMSE) quantify the temporal deviations (in years) between the estimated and reference construction periods, with the latter assigning a higher penalty to larger temporal discrepancies. For validation, 90 building sample points were randomly selected annually for each study area, yielding a total of 3600 validation points across the two metropolitan regions over the 20-year study period. Both direct and indirect verification protocols were executed via the Google Earth Engine (GEE) platform, with approximately

70% of the reference samples directly interpreted from high-resolution historical imagery and approximately 30% supported by NDVI-assisted verification in data-gap cases, as described in Section 2.2.3. The final evaluation metrics are synthesized in Tables 2 and 3, and the corresponding confusion matrices.

Table 2. Annual classification accuracy metrics (PA and UA) for building construction timelines in Shenzhen and Hanoi from 2001 to 2020 derived from randomly stratified validation samples.

Year	Shenzhen (PA %)	Shenzhen (UA %)	Hanoi (PA %)	Hanoi (UA %)
2001	92.59	83.33	96.15	83.33
2002	83.15	78.72	89.41	84.44
2003	82.02	81.11	92.68	84.44
2004	85.23	83.33	88.64	86.67
2005	88.24	83.33	90.59	84.62
2006	90	80	90.7	86.67
2007	89.16	82.22	90.8	87.78
2008	86.05	82.22	90.24	82.22
2009	91.57	84.44	83.16	88.76
2010	94.05	87.78	91.36	80.43
2011	86.05	86.05	89.77	83.16
2012	83.33	83.33	87.64	84.78
2013	87.36	84.44	88.64	87.64
2014	83.33	77.78	92.77	85.56
2015	85.71	80	90.59	85.56
2016	85.54	78.89	94.05	87.78
2017	87.21	83.33	96.34	87.78
2018	82.35	77.78	90.36	83.33
2019	85.88	81.11	92.77	85.56
2020	92.77	85.56	96.34	87.78

Table 3. Overall statistical accuracy metrics for chronological building construction prediction in Shenzhen and Hanoi.

City	Overall Accuracy	Mean Absolute Error	Root Mean Squared Error
Shenzhen	81.61%	0.22 years	0.58 years
Hanoi	85.06%	0.17 years	0.51 years

For the empirical evaluation in Shenzhen, China, the summary statistics in Table 3 reveal an overall accuracy of 81.61%, accompanied by tight temporal offsets characterized by an MAE of 0.22 years and an RMSE of 0.58 years, demonstrating a robust capacity to capture fine-grained urban dynamics. As detailed in Table 2 and the confusion matrix in Figure 9a, the annual PA and UA values consistently remained stable, hovering predominantly above 80% throughout the 2001–2020 timeline. Peak classification performance was recorded in 2010, where the PA reached 94.05% and the UA reached 87.78%, corresponding to 79 correctly identified sample points along the diagonal of the confusion matrix. In contrast, minor performance fluctuations were observed in specific years, notably in 2014 (PA of 83.33%, UA of 77.78%) and in 2018 (PA of 82.35%, UA of 77.78%). The confusion matrix clarifies that these localized reductions in efficiency were primarily driven by temporal displacement into adjacent years—such as the 4 and 5 sample points from 2014 mistakenly assigned to 2013 and 2015, respectively—alongside a minor portion of pixels remaining unclassified in the "Unclear" category due to intensive spectral mixing or persistent cloud cover. Nevertheless, the constrained margins of the MAE and RMSE underscore that the proposed framework reliably resolved the construction timelines for Shenzhen, validating the theoretical framework under complex urban environments.

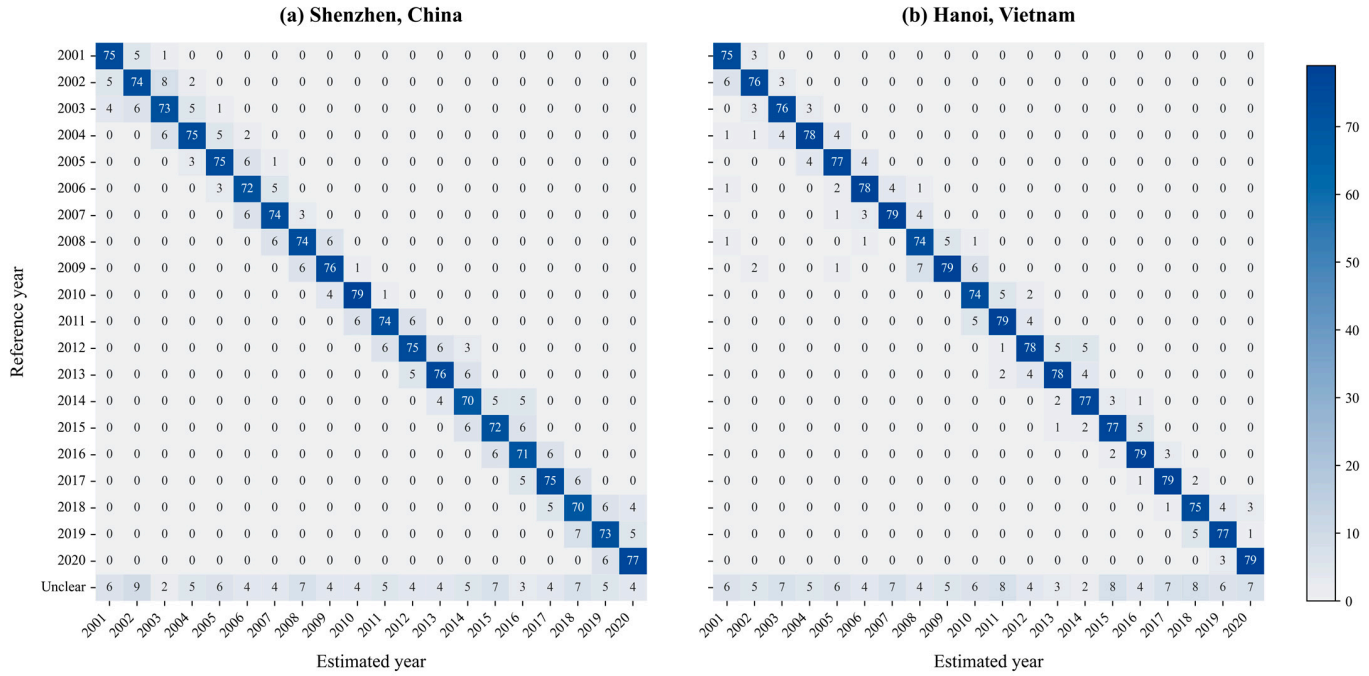


Figure 9. Annual confusion matrices evaluating the chronological prediction accuracy of the proposed framework over the 2001–2020 timeline: (**a**) Shenzhen, China; and (**b**) Hanoi, Vietnam.

Simultaneously, the building classification framework for Hanoi, Vietnam, demonstrated an equally robust classification efficacy, yielding an overall accuracy of 85.06% accompanied by a localized temporal offset characterized by an MAE of 0.17 years and an RMSE of 0.51 years, with the latter slightly penalizing occasional larger outliers in temporal prediction. The yearly breakdown in Table 2 highlights a highly consistent performance across the analytical timeline, with the framework achieving its peak Producer's Accuracy (PA) in 2001 (96.15%), as well as in 2017 and 2020 (both reaching 96.34%), while maintaining strong performance in other years such as 2016 (94.05%) and 2019 (92.77%). The confusion matrix in Figure 9b corroborates this evaluation, showing that the framework secured exactly 79 correct classifications along the diagonal in the years 2007, 2009, 2016, 2017, and 2020, and maintained 78 correct classifications in 2004, 2006, 2012, and 2013. A minor localized fluctuation occurred in 2008, where the UA dropped to 82.22% primarily because 7 sample points from the reference year of 2008 were temporally misclassified into 2009, inducing a higher commission error for that specific cohort. Despite these minor annual fluctuations and adjacent-year cross-talk, the consistently high PA and UA values combined with the constrained overall MAE confirm that the proposed framework possesses strong cross-border generalization and high stability in inferring building construction timelines across contrasting geographical and urban settings.

3.2. Qualitative Validation

In order to verify the effectiveness of the proposed framework in determining building construction periods, official archival records documenting the construction initiation dates for selected buildings in Shenzhen, China, were collected to serve as a reliable reference baseline. The operational fidelity of the methodology was further cross-validated using historical remote sensing data available through Google Earth. The direct verification against the actual conditions of buildings with clearly documented completion dates in Shenzhen constituted the core and most rigorous validation approach within this study.

Focusing first on Shenzhen University Town (Xili), this master-planned development is situated in the northeastern part of Nanshan District, contiguous to Shenzhen Safari

Park and approximately 10 km from the Shenzhen High-tech Industrial Park. The total planned construction area spans 10 square kilometers, with the first phase covering 3.8 square kilometers divided into eastern and western campuses, of which 1.54 square kilometers have been fully institutionalized and commissioned. Infrastructural development of the university town commenced in 2002, and by September 2003, the basic teaching infrastructure was largely completed and operational. By the end of 2016, the cumulative built-up area of the western campus had reached 508,900 square meters. The localized classification result for this area is presented in Figure 10a.

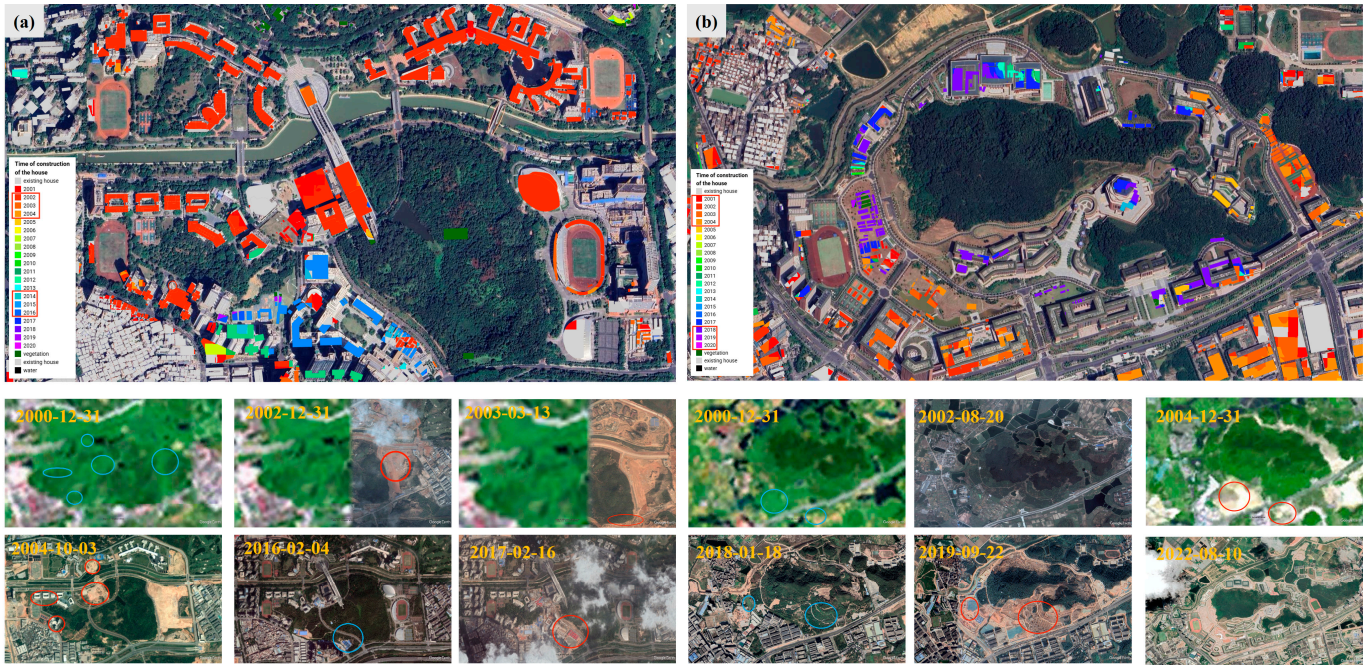


Figure 10. Site-specific validation of reconstructed building construction timelines against multi-temporal historical imagery for selected institutional subregions in Shenzhen: (**a**) Shenzhen University Town (Xili); and (**b**) Shenzhen Campus of Sun Yat-sen University. For each subregion, the upper panel displays the localized chronological inversion results yielded by the proposed framework, while the lower panel presents the corresponding synchronous Google Earth historical reference imagery, with the acquisition dates annotated in the upper-left corners.

Analysis revealed that the majority of buildings within this area were confirmed as having been constructed in 2002, while a cluster of buildings in the southern part exhibited construction activity concentrated primarily within the period from 2011 to 2016. Through a comparative analysis of the period from 2000 to 2002, as depicted in Figure 10, changes from the image of 31 December 2002 to the image of 13 March 2003 in Figure 10a can be observed, whereby a previously vegetated area was systematically converted to cleared land and prepared for subsequent structural deployment by the end of 2002. The model employed in this study effectively captured this transition process, identifying the initiation of surface disturbance in this area between 2001 and 2002, which is consistent with the expected monitoring outcome.

Furthermore, observational data from the image of 31 December 2002 to the image of 13 March 2003 in Figure 10a indicate that the area marked by the red circle remained vegetated at the end of 2002 but had been transformed into a built-up area by 2004. According to the model detection results, this change commenced in 2003. Given the temporal resolution limitations of the Google Earth imagery and the constraints of actual building construction cycles, it is reasonable to infer that these parcels underwent greenfield clearance in 2003, with vertical structural completion finalized in the subsequent year of 2004. After

completing the analysis of the initial construction phase, the study further examined the construction situation in the lower-left sector, where construction activity was monitored between 2011 and 2016. A comparison of the image of 4 February 2016 to the image of 16 February 2017 in Figure 10a clearly shows that most of the construction work in the core infrastructural build-out in this sector area had been completed before 2016. Notably, the area marked by a red circle experienced a major transition from vegetation cover to building cover between 2016 and 2017. The model adopted in this study identified this vegetation change as occurring in 2016 and accordingly designated it as the start year of building construction for this area. This determination is not only consistent with actual observations but also provides strong verification of the methodology's temporal fidelity. The analysis then moved to the Shenzhen campus of Sun Yat-sen University, located at No. 66 Gongchang Road, Guangming District, Shenzhen. The campus has a total planned territorial land area of 314.3 hectares and a first-phase construction area of 144.82 hectares. The cumulative structural gross floor area is approximately 2.2 million square meters, constructed in two phases. Comprehensive construction work began on 12 June 2018, with delivery planned in two batches in 2020 and 2021, while the remaining approximately 930,000 square meters of buildings were scheduled for completion in 2021. By June 2023, the first phase of the Shenzhen campus was fully completed. The final classification result for this area is presented in Figure 10b.

When the model was applied to this campus, the results shown in Figure 10 revealed that construction activities in the lower-left corner were predominantly concentrated during the 2002 to 2005 period, whereas construction in the upper-right corner was mainly concentrated between 2018 and 2020.

Focusing first on the lower-left corner, a comparison between the image acquired on 31 December 2000 and the image acquired on 31 December 2004 in Figure 10b clearly shows that this area transitioned from vegetation cover to a built-up area between 2000 and 2004. This change indicates that buildings have stood in this area since that time, and subsequent remote sensing imagery confirms that the area has consistently maintained built-up characteristics without undergoing vegetation restoration.

It can thus be inferred that when construction of the Sun Yat-sen University Shenzhen campus commenced in 2018, this area only involved the demolition and reconstruction of existing old buildings. The NDVI of this area remained consistently at the level typical for built buildings, and the model only identified the time point of the initial building construction in this area, and recorded the building-level NDVI that persisted thereafter.

Further spatiotemporal analysis demonstrates that the main construction activities of the Sun Yat-sen University Shenzhen campus occurred after vegetation clearance. The proposed model exhibited remarkable sensitivity in capturing these abrupt land cover changes, particularly during the validation period from 2018 to 2020. When combined with the official construction schedule and multi-temporal image data, the model accurately identified the transition from vegetated surfaces to early building structures during the period from January 2018 to September 2019. These results, validated in areas with complete development timeline records, strongly demonstrate the reliability of the framework in accurately pinpointing the commencement of construction activities.

3.3. Comparative Analysis with Existing Approaches

To evaluate the effectiveness of the proposed annual composite strategy, comparative analyses were conducted against two approaches representing different methodological paradigms in building age mapping.

3.3.1. Qualitative Comparison with BATSCCD

BATSCCD (Zhuo et al., 2024) represents a state-of-the-art approach that likewise leverages the multi-decadal Landsat archive for building age retrieval [21]. It adopts a data-intensive strategy, exploiting full-band spectral information and a Random Forest classifier to resolve high-dimensional features of land cover change. While theoretically capable of identifying multiple change types, this strategy encounters substantial practical bottlenecks in persistently cloudy or cloud-prone regions. The reliance on consistent multi-band signals makes RF-based models propagated noise from cumulative atmospheric artifacts, and the requirement for large volumes of high-quality training labels across different time periods introduces non-negligible risks of model drift when reference data are temporally biased or sparse.

In contrast, the proposed TTM framework adopts a parsimonious strategy focused on the robust identification of a single, physically grounded transition type—the vegetation-to-impervious NDVI signature. This rule-driven matching logic circumvents the prerequisite for large-scale training annotations and exhibits enhanced resilience to spectral noise arising from residual atmospheric contamination. The choice between these two paradigms ultimately hinges on the application context: BATSCCD is well suited for data-rich environments where comprehensive training data can be compiled, whereas the TTM framework is purposely engineered for resource-constrained and data-scarce settings where simplicity and robustness are prioritized. A full quantitative comparison would require re-training the RF classifier under identical data conditions across all study sites, which extends beyond the scope of this baseline manuscript and is highly encouraged for future scholarly exploration.

3.3.2. Quantitative Comparison with Monthly NDVI-Based Approach

A quantitative comparison was conducted with the method proposed by Hu et al. (2024) [11], representing one of the few contemporary benchmarks specifically engineered for building construction year retrieval using monthly Landsat time series within the LandTrendr temporal segmentation framework. The comparison was designed to test a specific hypothesis: whether the annual composite strategy, which deliberately sacrifices monthly temporal granularity, offers measurable advantages in robustness under cloud-prone conditions.

To first diagnose the spatial explicitly patterns and failure modes at a fine scale, a representative sub-region containing 47 buildings was analyzed in detail (Figure 11, Table 4). In this sub-region, the proposed method correctly identified 39 buildings (PA = 0.83), compared with 16 buildings (PA = 0.34) for the monthly approach. Per-building inspection (Figure 11) revealed a systematic failure mode in the monthly method. A substantial fraction of buildings were chronologically misassigned to epochs far outside the actual construction window: Buildings 2 and 8 (reference window: 2016–2018) were back-dated to 2001; Building 21 (reference window: 2016–2018) was classified to 2002; and Building 45 (reference window: 2018–2020) was classified to 1998. These discrepancies of 15–20 years are inconsistent with gradual urban development and are best explained by cloud-induced artifacts corrupting the monthly NDVI signal. Furthermore, several buildings in the sub-region (e.g., Buildings 3, 4, 6, 8) yielded unclassifiable or ambiguous signals under the monthly approach, which the LandTrendr framework nonetheless assigned a classification year due to the absence of an explicit confidence thresholding mechanism.

Building on this sub-region diagnosis, the analysis was scaled up to a city-wide validation. A set of buildings with clearly documented construction timelines in Shenzhen was selected as validation samples. The construction years of these buildings were manually delineated through visual interpretation of high-resolution Google Earth time-series imagery

(Figure 11). The labeling protocol identified the year in which vegetation clearing or distinct vertical structural features first materialized at a given location, which was recorded as the construction start year. After rigorous screening to exclude ambiguous cases, a total of 285 buildings were confirmed as the validation set (Figure 12).

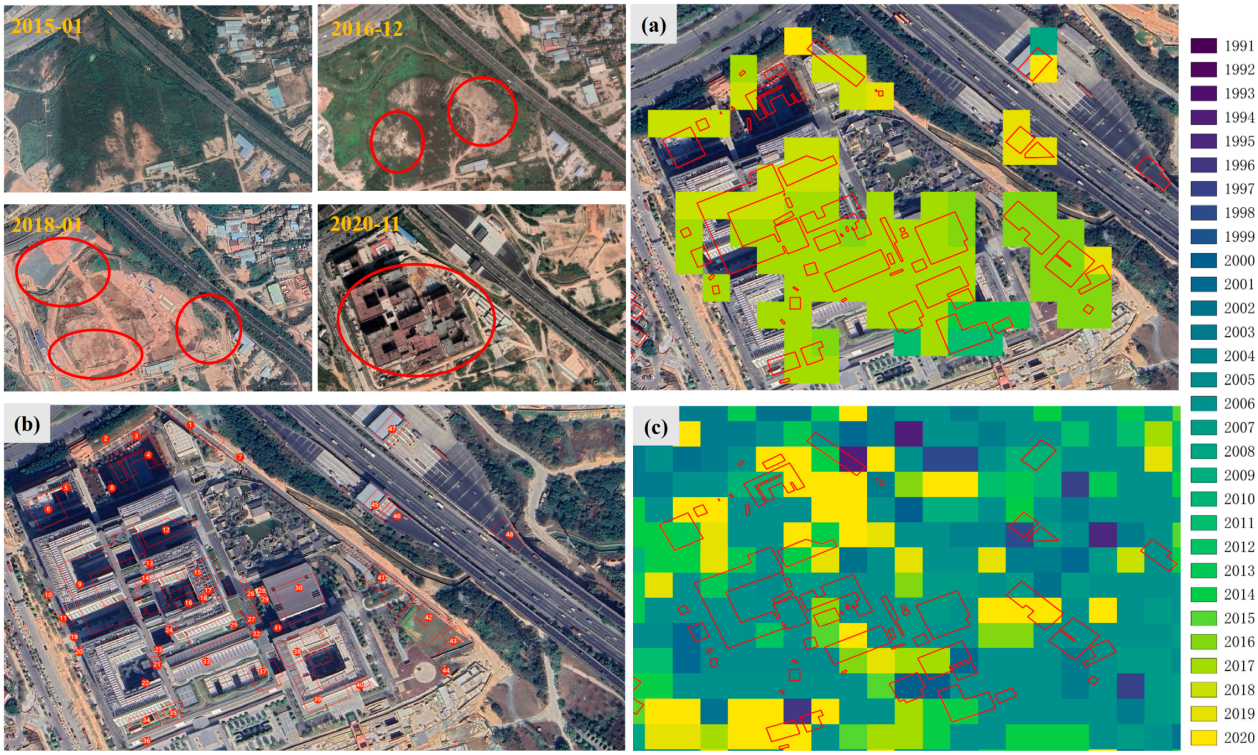


Figure 11. Micro-scale comparative analysis of historical building construction year retrieval within the representative sub-region: (**a**) localized chronological inversion results yielded by the proposed TTM framework; (**b**) manual reference ground-truth boundaries delineated via multi-temporal Google Earth interpretation; and (**c**) chronological extraction results derived from the monthly LandTrendr-based contemporary benchmark (Hu et al., 2024 [11]). For each panel, the respective synchronous high-resolution Google Earth satellite reference imagery is integrated as the visual baseline, with the precise overpass acquisition dates annotated in the upper-left corners.

Table 4. Comparison of the accuracy of the prediction results of the two models for small regions.

Overall Target Number of Small Regions	Number of Successful Predictions in This Model	Hu et al. Model Successfully Predicts Results
47	39	16
PA	0.83	0.34

Because the contemporary benchmark developed by Hu et al. logs building construction timelines at a monthly temporal resolution whereas the proposed framework operates on an annual baseline, the monthly chronological outputs were systematically aggregated into annual construction cohorts to ensure a mathematically equitable and rigorous cross-comparison. Both methodological paradigms were deployed across the definitive 285-building independent validation set in Shenzhen. The proposed annual composite TTM framework correctly resolved the exact construction initiation years for 238 out of the 285 reference targets, yielding a robust Producer's Accuracy (PA) of 83.51% (conventionally indexed as 0.84). Conversely, the monthly LandTrendr-based segmentation method achieved only 133 correct historical identifications, corresponding to a compromised PA of 46.67% (Table 5). This substantial performance discrepancy—amounting to a net gain of

105 correctly isolated building structures—provides definitive, empirical validation that the proposed annual composite strategy offers decisive advantages in sustaining operational robustness across cloud-prone urban environments.

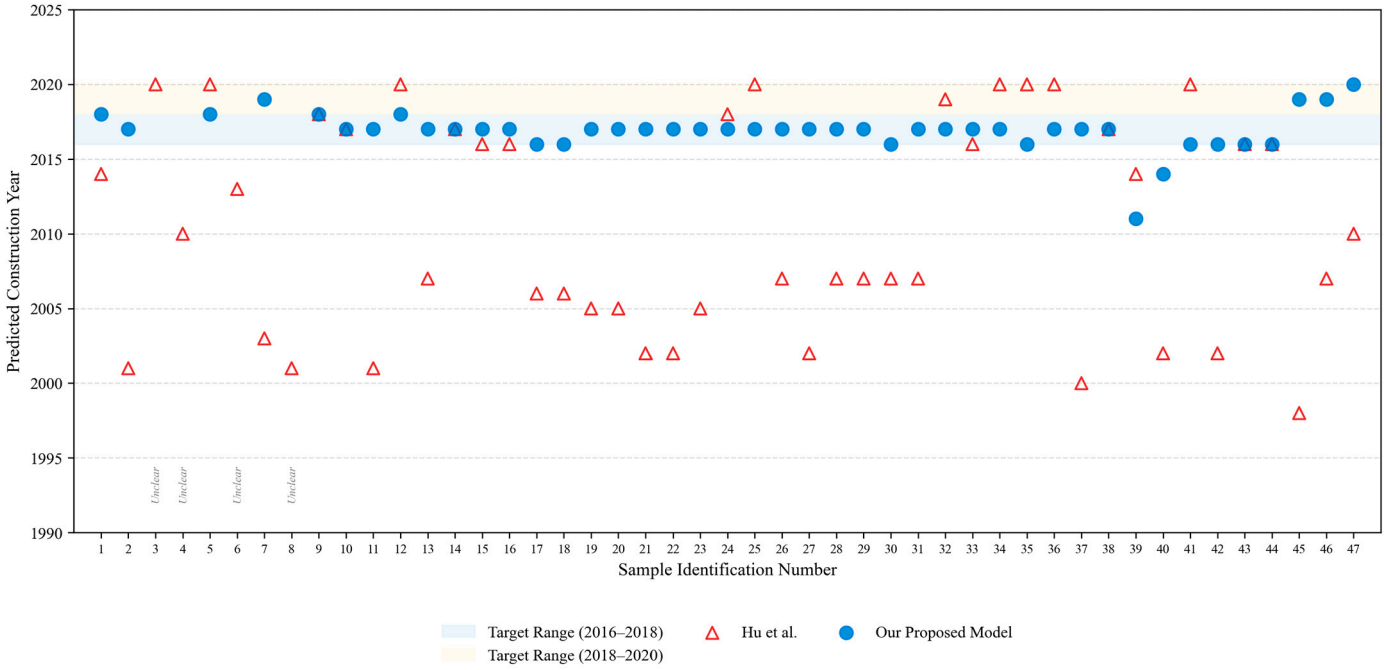


Figure 12. Accuracy comparison of predicted construction years for 47 validation samples. The plot evaluates our proposed model (blue circles) against the baseline by Hu et al. (2024) [11] (red triangles), with shaded bands indicating target ground truth ranges. Our model demonstrates higher temporal precision by consistently aligning with the target windows, while "Unclear" labels denote samples with uncertain historical transition dates.

Table 5. Comparison of Model Accuracy in Shenzhen.

Overall Target Number	Number of Successful Predictions in This Model	Hu et al. Model Successfully Predicts Results
285	238	133
PA	0.84	0.47

The observed performance gap can be attributed to a fundamental difference in how the two methodological paradigms mitigate temporal data scarcity. The monthly LandTrendr-based approach is contingent upon a sufficiently dense multi-temporal stack of cloud-free observations to reliably detect the inflection point marking construction onset. In Shenzhen, which is characterized by a humid subtropical monsoon climate, persistent cloud cover during the growing season frequently reduces the number of usable monthly observations below the critical threshold required for stable algorithm performance. The resulting data gaps introduce spurious, high-frequency fluctuations into the intra-annual NDVI time series that are highly susceptible to being misinterpreted as land-cover mutation events, leading to false detections or gross temporal misattributions.

In contrast, the proposed annual composite strategy circumvents this vulnerability by synthesizing all available cloud-free observations within each year—and, through the rolling window, leveraging data from contiguous years—into a single, stable NDVI value. This integration substantially suppresses the high-frequency noise that dominates the monthly signal, yielding a significantly refined characterization of the long-term spectral

trajectory. The annual signal is admittedly coarser in temporal resolution but exhibits far higher fidelity to the true underlying land cover state.

These results do not constitute a general critique of LandTrendr-based approaches, which have demonstrated robust capabilities within their designated application contexts, particularly in less cloud-affected geographical environments. Rather, they provide robust empirical support for the central design premise of the proposed framework: in cloud-rich tropical and subtropical environments, a strategy that prioritizes annual data integrity over monthly temporal granularity can yield substantially more reliable construction-year estimates.

4. Discussion

4.1. A Robust Framework for Mapping the Foundational Layer of Physical Vulnerability

This study established a robust and deliberately parsimonious methodological architecture for reconstructing building construction years by integrating cloud-free annual Landsat NDVI composites with open-source building footprints. The framework's core design principle—strategically trading high-frequency monthly temporal granularity for long-term annual data integrity—proved highly effective across two heterogeneous cities spanning diverse climatic and developmental contexts. Across all experimental sites, the annual composite-based TTM algorithm maintained a stable Producer's Accuracy (PA) strictly above 80.00%, substantially outperforming the monthly LandTrendr-based segmentation contemporary benchmark (PA = 46.67%, as indexed in Table 5). This consistent performance under persistent cloud contamination validates the central premise of our approach: in temporal observation-scarce environments, a coarser but significantly refined annual spectral signal exhibits far greater resilience than finer-grained but noise-sensitive multi-temporal alternatives.

The practical significance of this finding extends beyond a mere methodological preference. What the framework generates—building-level construction year estimates across entire urban agglomerations—constitutes an operational, baseline data layer for macro-scale physical vulnerability triage screening. As rigorously re-contextualized in the Introduction, a building's age functions as a hazard-agnostic preliminary proxy variable that indirectly encodes historical structural design standards, material degradation trajectories, and cumulative structural aging. Without this foundational layer, subsequent multi-tier vulnerability modeling—whether for seismic micro-zonation risk, hydrodynamic flood exposure, or wind-load assessment—lacks the essential spatial input regarding the built environment's physical condition. The classification maps produced for the two study cities make this tangible: for the first time, these metropolitan areas possess spatially explicit, building-level age data that can distinguish between recent construction built to modern building safety codes and older building stock likely erected under less stringent or absent regulatory standards.

Beyond the absolute accuracy figures, the comparative analysis (Section 3.3) revealed a deeper epistemic insight about methodological choice under severe data constraints. The monthly LandTrendr-based method did not exhibit stochastic error propagation; rather, it unmasked a systematic failure mode in which cloud-induced discontinuities within the high-frequency temporal record generated spurious, intra-annual NDVI volatility. These artifacts were highly susceptible to being misinterpreted as land-cover mutation events, leading to gross temporal misattributions—erroneously back-dating building structures constructed between 2016 and 2018 to epochs as chronologically distant as 2001 or 1998. This failure pattern is not a reflection on the LandTrendr algorithm per se, but a consequence of applying a high-frequency detection paradigm to an environment where the required observation density cannot be physically sustained. The annual composite strat-

egy circumvents this vulnerability not through hyper-parameter algorithmic sophistication, but through a design choice that matches the temporal resolution of the analysis to the effective information content of the available data. This principle—aligning methodological complexity with contextual data richness—carries profound implications extending beyond the specific scope of building infrastructure retrieval and directly informs remote sensing time-series analysis in other persistently cloud-prone geographical regions.

The framework's deliberate simplicity—built exclusively on publicly available Landsat archives and open-source building footprints, requiring no proprietary datasets or specialized hardware—directly addresses the implementation barriers that have historically prevented the generation of building-age data in resource-constrained settings. The qualitative comparison with BATSCCD (Section 3.3.1) further contextualizes this design philosophy: data-intensive approaches exploiting full-band spectral architectures alongside machine learning classifiers offer theoretical advantages in capturing heterogeneous land-cover dynamics, but their practical deployment in cloud-prone, data-scarce regions encounters substantial practical bottlenecks related to historical training annotation availability, cross-period model drift, and structural sensitivity to atmospheric noise. The choice between these paradigms is ultimately context-dependent, and the TTM framework is specifically optimized for scenarios where operational robustness, deterministic logic, and institutional ease of deployment are prioritized over maximal multi-spectral feature extraction.

4.2. Policy Implications for Resilient Urban Planning

The building-age mapping framework developed in this study serves as an operational, macro-scale spatial triage tool for urban resilience planning, rather than a deterministic indicator of absolute structural vulnerability. For rapidly expanding Global South cities lacking standardized municipal inventories, this remote sensing methodology offers a cost-effective, rapidly deployable first-pass sorting mechanism. By resolving construction chronology at the individual footprint level, it enables decision-makers to visually diagnose the distribution of potentially high-vulnerability building stock—specifically delineating structural cohorts erected before the enforcement of modern seismic and structural codes. This localized intelligence helps municipal authorities optimize limited fiscal resources by systematically directing detailed engineering inspections, on-site material testing, and targeted retrofitting subsidies toward the most critical urban sectors.

As a hazard-agnostic baseline, this chronological dataset can inform heterogeneous risk domains—such as seismic micro-zonation, hydrodynamic inundation modeling, and urban heat island susceptibility—depending on the local hazard profile. This versatility is exceptionally valuable in resource-constrained settings, where a singular building-age layer can anchor initial multi-hazard screenings before cost-intensive, hazard-specific engineering simulations are formally commissioned. Within a comprehensive mitigation pipeline, this layer acts as "Layer 0" screening metadata, designed to be incrementally coupled with local building-code histories, material typologies, and disaster loss databases. Integrating this baseline with high-resolution hazard exposure maps and climate projections facilitates a shift from static risk mapping to dynamic forecasting. Planners can thus simulate how historical building cohorts would be exposed under projected floodplain expansions or elevated seismic hazard levels, informing both near-term reinforcement staging and long-term land-use zoning policies.

The capacity of this framework to isolate vulnerability patterns linked to distinct construction epochs carries direct policy relevance. In hyper-urbanizing cities, historical waves of peak construction often coincide with regulatory or political transitions when safety codes were either nascent or inadequately enforced. Buildings produced during

these institutional windows constitute a systematically elevated risk cohort. By translating construction years into an actionable, georeferenced policy target at the building scale, this framework provides an empirical baseline to delineate hidden structural risks. This represents a fundamental pivot from reactive post-disaster response toward proactive pre-disaster risk reduction, directly advancing the global targets of the Sendai Framework for Disaster Risk Reduction. Moving forward, we recommend incorporating building age as a standard preliminary sorting layer into institutionalized risk assessment architectures, ultimately establishing a rigorous, scientific baseline for municipal retrofit prioritization and the empirical calibration of future resilient design criteria.

4.3. Methodological Considerations and Limitations

Several aspects of the proposed framework outline its current scope and point toward meaningful directions for future refinement, without diminishing the validity of the findings presented here. The framework relies primarily on NDVI, which is well-suited for capturing vegetation-to-impervious transitions that dominated the historical expansion of Hanoi and Shenzhen, but less effective for non-vegetated conversions such as brownfield redevelopment. Nevertheless, historical land-use patterns indicate that the proportion of such non-vegetated transformations remains relatively low within our study areas, meaning this limitation does not compromise the macro-scale applicability of our method. To address low baseline contrast and the inherent mixed-pixel challenges of 30 m Landsat data in hyper-dense blocks, we utilized vector building footprints as prior structural constraints and a majority voting scheme; however, uncertainties remain for structures smaller than a pixel. Future iterations will explore multi-sensor fusion with higher-resolution constellations (e.g., Sentinel-2 or PlanetScope) and incorporate complementary indices (e.g., NDBI). Furthermore, while our annual compositing strategy minimizes cloud contamination, persistent cloud cover in subtropical regions can still cause residual gaps, and the rolling composite design introduces a deliberate 1-to-2-year temporal lag to trade near-real-time capability for temporal robustness. Regarding methodological benchmarking, direct empirical comparisons with pixel-based algorithms (e.g., CCDC, BFAST, LandTrendr), BATSCCD, or emerging deep learning models were constrained by substantial computational overhead, parameter-tuning complexity, and the lack of standardized validation datasets. To overcome these barriers, we plan to actively pursue open-source benchmarking initiatives in our future work, evaluating the TTM framework against these mainstream algorithms under identical cloud-filtering scenarios to establish a standardized baseline for the community. Establishing a systematic accuracy assessment stratified by footprint sizes and land-cover typologies under identical cloud-filtering scenarios remains a critical avenue for future collaborative validation. Finally, the current model focuses on construction timing rather than inferring functional use or subsequent occupancy, which could be enriched in future work by integrating ancillary data like nighttime lights or morphological metrics. We also acknowledge that while quantitative metrics were robustly reported for both sites, the qualitative visual presentation was primarily focused on Shenzhen; future efforts will expand localized visual showcases across a wider array of global urban forms and cross-border climatic zones. Ultimately, these acknowledged limitations do not diminish the framework's demonstrated utility for generating essential first-order building-age data in data-scarce regions.

5. Conclusions

Accurately determining the construction year of individual buildings is fundamental to assessing urban physical vulnerability—yet it remains a formidable challenge in temporal data-scarce and cloud-prone regions where conventional high-frequency remote

sensing methods systematically fail. This study addressed this persistent empirical gap by proposing a robust and deliberately parsimonious methodological framework that reconstructs building age by integrating cloud-free annual Landsat NDVI composites with open-source building footprints.

The framework's core design principle—strategically trading high-frequency monthly temporal granularity for long-term annual data integrity—was rigorously validated across a dual-city comparative framework spanning distinct socio-economic and developmental trajectories (Shenzhen, China and Hanoi, Vietnam). Validated against the rigorous reference baseline dataset, the proposed annual composite-based Temporal Template Matching (TTM) algorithm achieved a stable Producer's Accuracy (PA) of 83.51% (conventionally indexed as 0.84), substantially outperforming the monthly LandTrendr-based segmentation contemporary benchmark (PA = 46.67%, as indexed in Table 5). These results demonstrate that in persistently cloudy environments, a coarser but significantly refined annual spectral signal exhibits far greater resilience than finer-grained but noise-sensitive multi-temporal alternatives. The comparative analysis further revealed that the monthly approach does not fail randomly but unmasks a systematic vulnerability to cloud-induced spatiotemporal discontinuities within the temporal record, which the annual compositing strategy effectively circumvents not through hyper-parameter sophistication, but through a design choice that aligns the analytical scale with effective information content.

Beyond this methodological finding, the framework generates a critical spatial data product: building-level construction year estimates that serve as an operational, baseline data layer for macro-scale physical vulnerability triage screening. As rigorously re-contextualized to ensure structural engineering alignment, a building's age functions as a hazard-agnostic preliminary proxy variable that indirectly encodes historical structural design standards, building-code enforcement epochs, material degradation trajectories, and cumulative structural aging. Without this foundational database, subsequent multi-tier vulnerability modeling—whether for seismic micro-zonation risk, hydrodynamic flood exposure, or wind-load assessment—lacks the essential spatial input regarding the built environment's physical condition. The framework enables vulnerability triage—the macro-scale spatial sorting of potential building cohorts most likely to require detailed structural intervention—across entire urban agglomerations. For cities in the Global South that lack comprehensive institutional building inventories, this represents previously unavailable intelligence for prioritizing limited municipal resources toward subsequent, resource-intensive phases including detailed on-site inspection and expert engineering assessments.

The framework's deliberate simplicity is central to its value proposition. Built entirely on publicly available satellite data archives and open-source building footprints, requiring no proprietary datasets, specialized hardware, or extensive training annotations, it directly addresses the implementation barriers that have historically prevented building-age data generation in resource-constrained settings. The successful validation across the dual metropolitan regions characterized by highly distinct urban morphologies, development histories, and dense institutional footprints provides empirical evidence for the framework's scalability and suggests that the underlying "vegetation-to-impervious" transition deterministic logic generalizes robustly across diverse urban horizontal expansion patterns.

Several limitations define the boundaries of the current contribution and indicate directions for future work. The reliance on NDVI makes the method most effective for vegetation-to-impervious transitions and less sensitive to construction on non-vegetated land; the 30 m Landsat resolution constrains detection in extremely dense urban cores; and the rolling composite design trades near-real-time capability for historical robustness. Extending the validation to a wider range of urban contexts, integrating post-2015 Sentinel-2 data for improved recent-construction detection, and benchmarking against emerging

deep learning approaches as they mature for multi-sensor Landsat archives represent logical next steps.

By providing a scalable, computationally lightweight, and rigorously validated methodology for generating building-age data in regions where such data have never existed, this work offers a practical tool for shifting urban governance from reactive post-disaster response toward proactive, data-informed vulnerability reduction—directly supporting the objectives articulated in the Sendai Framework for Disaster Risk Reduction.

Author Contributions: Conceptualization, Y.L., X.Z. and Q.Z.; methodology, Y.L., Z.M. and Q.Z.; investigation: Y.L.; writing—original draft preparation, Y.L. and Q.Z.; writing—review and editing, Y.L. and Q.Z.; visualization, Y.L., X.Z., Q.Z. and Z.M.; supervision, Q.Z. and Z.W.; project administration, Q.Z. and Z.W.; funding acquisition, Q.Z. All authors have read and agreed to the published version of the manuscript.

Funding: This work was supported in part by the Shenzhen Key Laboratory of Intelligent Microsatellite Constellation (No. ZDSYS20210623091808026), the Open Research Fund of the Science and Technology Innovation Platform of Changsha University of Science and Technology (No. 2025ZKPT057), the Hunan Provincial Natural Science Foundation of China (No. 2026JJ60618), and the Hunan Engineering Technology Research Center of Natural Resources Survey and Monitoring (No. 2018TP2040).

Data Availability Statement: The raw data supporting the conclusions of this article will be made available by the authors on request.

Conflicts of Interest: The authors declare no conflicts of interest.

References

1. Saja, A.A.; Teo, M.; Goonetilleke, A.; Ziyath, A.M. A critical review of social resilience properties and pathways in disaster management. *Int. J. Disaster Risk Sci.* **2021**, *12*, 790–804. [CrossRef]
2. Ner, N.T.; Okyere, S.A.; Abunyewah, M.; Kita, M. Integrating resilience attributes into local disaster management plans in Metro Manila: Strengths, weaknesses, and gaps. *Prog. Disaster Sci.* **2022**, *16*, 100249. [CrossRef]
3. Hofmann, S.Z. 100 Resilient Cities program and the role of the Sendai framework and disaster risk reduction for resilient cities. *Prog. Disaster Sci.* **2021**, *11*, 100189. [CrossRef]
4. Greiving, S.; Schödl, L.; Gaudry, K.-H.; Quintana Miralles, I.K.; Prado Larraín, B.; Fleischhauer, M.; Jácome Guerra, M.M.; Tobar, J. Multi-risk assessment and management—A comparative study of the current state of affairs in Chile and Ecuador. *Sustainability* **2021**, *13*, 1366. [CrossRef]
5. Quesada-Román, A. Disaster risk assessment of informal settlements in the Global South. *Sustainability* **2022**, *14*, 10261. [CrossRef]
6. Petzold, J.; Scheffran, J. Climate change and human security in coastal regions. *Camb. Prism. Coast. Futures* **2024**, *2*, e5. [CrossRef] [PubMed]
7. Hussainzad, E.A.; Gou, Z. Climate risk and vulnerability assessment in informal settlements of the global south: A critical review. *Land* **2024**, *13*, 1357. [CrossRef]
8. Dodman, D.; Hayward, B.; Pelling, M.; Castán Broto, V.; Chow, W.; Chu, E.; Dawson, R.; Khirfan, L.; McPhearson, T.; Prakash, A.; et al. Cities, settlements and key infrastructure. In *Climate Change 2022: Impacts, Adaptation and Vulnerability*; Cambridge University Press: Cambridge, UK; New York, NY, USA, 2023.
9. Elqudah, S.M.; Vigh, L.G. Coexisting with Disasters: A State-of-the-art Review of Resilience Assessment of Steel Structures under Extreme Hazards. *Period. Polytech. Civ. Eng.* **2025**, *69*, 1187–1202. [CrossRef]
10. Meyers-Angulo, J.E.; Martinez-Cuevas, S.; Gaspar-Escribano, J.M. Classifying buildings according to seismic vulnerability using Cluster-ANN techniques: Application to the city of Murcia, Spain. *Bull. Earthq. Eng.* **2023**, *21*, 3581–3622. [CrossRef]
11. Hu, T.; Zhang, M.; Li, X.; Wu, T.; Ma, Q.; Xiao, J.; Huang, X.; Guo, J.; Li, Y.; Liu, D. Extraction of Building Construction Time Using the LandTrendr Model with Monthly Landsat Time Series Data. *IEEE J. Sel. Top. Appl. Earth Obs. Remote Sens.* **2024**, *17*, 18335–18350. [CrossRef]
12. Tsiavos, A.; Amrein, P.; Bender, N.; Stojadinovic, B. Compliance-based estimation of seismic collapse risk of an existing reinforced concrete frame building. *Bull. Earthq. Eng.* **2021**, *19*, 6027–6048. [CrossRef]
13. Dilena, M.; Dell'Oste, M.F.; Gubana, A.; Morassi, A.; Polentarutti, F.; Puntel, E. Structural survey of old reinforced concrete elevated water tanks in an earthquake-prone area. *Eng. Struct.* **2021**, *234*, 111947. [CrossRef]

14. Abdulqader, D.N.; Atrushi, D.S. Evaluation and Assessment of Existing Design Codes and Standards for Building Construction. *ARO-Sci. J. Koya Univ.* **2022**, *10*, 106–123. [CrossRef]
15. Mulas, M.G.; Stroffolini, L.; Martinelli, P. Vulnerability and retrofitting of torsionally deformable RC buildings: A case study. *Structures* **2021**, *32*, 861–875. [CrossRef]
16. Woldemichael, A.; Maduako, I. *Satellite-Based Census of Residential Buildings: Application for Climate Risk Assessment*; International Monetary Fund: Washington, DC, USA, 2024.
17. Biljecki, F.; Chow, Y.S.; Lee, K. Quality of crowdsourced geospatial building information: A global assessment of OpenStreetMap attributes. *Build. Environ.* **2023**, *237*, 110295. [CrossRef]
18. Xu, Y.; Wu, L.; Xie, Z.; Chen, Z. Building extraction in very high resolution remote sensing imagery using deep learning and guided filters. *Remote Sens.* **2018**, *10*, 144. [CrossRef]
19. Bittner, K.; Adam, F.; Cui, S.; Körner, M.; Reinartz, P. Building footprint extraction from VHR remote sensing images combined with normalized DSMs using fused fully convolutional networks. *IEEE J. Sel. Top. Appl. Earth Obs. Remote Sens.* **2018**, *11*, 2615–2629. [CrossRef]
20. Frantz, D.; Schug, F.; Okujeni, A.; Navacchi, C.; Wagner, W.; van der Linden, S.; Hostert, P. National-scale mapping of building height using Sentinel-1 and Sentinel-2 time series. *Remote Sens. Environ.* **2021**, *252*, 112128. [CrossRef] [PubMed]
21. Zhuo, L.; Huang, R.; Liao, C.; Tao, H.; Zang, Y. BATSCCD: A new change detection method for mapping building age in rapidly changing urban areas using Landsat time series data. *Int. J. Digit. Earth* **2024**, *17*, 2358859. [CrossRef]
22. Pasquarella, V.J.; Arévalo, P.; Bratley, K.H.; Bullock, E.L.; Gorelick, N.; Yang, Z.; Kennedy, R.E. Demystifying LandTrendr and CCDC temporal segmentation. *Int. J. Appl. Earth Obs. Geoinf.* **2022**, *110*, 102806. [CrossRef]
23. Kennedy, R.E.; Yang, Z.; Cohen, W.B. Detecting trends in forest disturbance and recovery using yearly Landsat time series: 1. LandTrendr—Temporal segmentation algorithms. *Remote Sens. Environ.* **2010**, *114*, 2897–2910. [CrossRef]
24. Verbesselt, J.; Hyndman, R.; Newnham, G.; Culvenor, D. Detecting trend and seasonal changes in satellite image time series. *Remote Sens. Environ.* **2010**, *114*, 106–115. [CrossRef]
25. Liu, C.; Zhang, Q.; Huang, H.; Xu, H.; Cheng, X. Identifying where and when urban renewal occurs: A continuous change detection-based framework using two decades' worth of Landsat data. *Int. J. Digit. Earth* **2025**, *18*, 2510573. [CrossRef]
26. Hansen, M.C.; Stehman, S.V.; Potapov, P.V.; Loveland, T.R.; Townshend, J.R.; DeFries, R.S.; Pittman, K.W.; Arunarwati, B.; Stolle, F.; Steininger, M.K. Humid tropical forest clearing from 2000 to 2005 quantified by using multitemporal and multiresolution remotely sensed data. *Proc. Natl. Acad. Sci. USA* **2008**, *105*, 9439–9444. [CrossRef] [PubMed]
27. Li, X.; Zhou, Y.; Zhu, Z.; Liang, L.; Yu, B.; Cao, W. Mapping annual urban dynamics (1985–2015) using time series of Landsat data. *Remote Sens. Environ.* **2018**, *216*, 674–683. [CrossRef]
28. Zhu, Z.; Woodcock, C.E. Continuous change detection and classification of land cover using all available Landsat data. *Remote Sens. Environ.* **2014**, *144*, 152–171. [CrossRef]
29. Wang, Y.; Liu, D.; Zhang, F.; Zhang, Q. Monitoring the spatio-temporal dynamics of shale oil/gas development with Landsat time series: Case studies in the USA. *Remote Sens.* **2022**, *14*, 1236. [CrossRef]
30. Wulder, M.A.; White, J.C.; Goward, S.N.; Masek, J.G.; Irons, J.R.; Herold, M.; Cohen, W.B.; Loveland, T.R.; Woodcock, C.E. Landsat continuity: Issues and opportunities for land cover monitoring. *Remote Sens. Environ.* **2008**, *112*, 955–969. [CrossRef]
31. Potere, D. Horizontal positional accuracy of Google Earth's high-resolution imagery archive. *Sensors* **2008**, *8*, 7973–7981. [CrossRef] [PubMed]
32. Yang, H.L.; Yuan, J.; Lunga, D.; Laverdiere, M.; Rose, A.; Bhaduri, B. Building extraction at scale using convolutional neural network: Mapping of the united states. *IEEE J. Sel. Top. Appl. Earth Obs. Remote Sens.* **2018**, *11*, 2600–2614. [CrossRef]
33. Sirko, W.; Kashubin, S.; Ritter, M.; Annkah, A.; Bouchareb, Y.S.E.; Dauphin, Y.; Keysers, D.; Neumann, M.; Cisse, M.; Quinn, J. Continental-scale building detection from high resolution satellite imagery. *arXiv* **2021**, arXiv:2107.12283. [CrossRef]
34. Chander, G.; Markham, B.L.; Helder, D.L. Summary of current radiometric calibration coefficients for Landsat MSS, TM, ETM+, and EO-1 ALI sensors. *Remote Sens. Environ.* **2009**, *113*, 893–903. [CrossRef]
35. Runge, A.; Grosse, G. Mosaicking Landsat and Sentinel-2 Data to Enhance LandTrendr Time Series Analysis in Northern High Latitude Permafrost Regions. *Remote Sens.* **2020**, *12*, 2471. [CrossRef]
36. Zhang, Q.; Li, B.; Thau, D.; Moore, R. Building a better urban picture: Combining day and night remote sensing imagery. *Remote Sens.* **2015**, *7*, 11887–11913. [CrossRef]
37. Kuang, W.; Liu, J.; Zhang, Z.; Lu, D.; Xiang, B. Spatiotemporal dynamics of impervious surface areas across China during the early 21st century. *Chin. Sci. Bull.* **2013**, *58*, 1691–1701. [CrossRef]
38. Agrawal, R.; Faloutsos, C.; Swami, A. Efficient similarity search in sequence databases. In Proceedings of the Foundations of Data Organization and Algorithms: 4th International Conference, FODO'93, Chicago, IL, USA, 13–15 October 1993; Proceedings 4, pp. 69–84.

39. Huang, C.; Goward, S.N.; Masek, J.G.; Thomas, N.; Zhu, Z.; Vogelmann, J.E. An automated approach for reconstructing recent forest disturbance history using dense Landsat time series stacks. *Remote Sens. Environ.* **2010**, *114*, 183–198. [CrossRef]
40. Steiner, J. The principles of majority and proportionality. *Br. J. Political Sci.* **1971**, *1*, 63–70. [CrossRef]

Disclaimer/Publisher's Note: The statements, opinions and data contained in all publications are solely those of the individual author(s) and contributor(s) and not of MDPI and/or the editor(s). MDPI and/or the editor(s) disclaim responsibility for any injury to people or property resulting from any ideas, methods, instructions or products referred to in the content.